

CARM1 drives mitophagy and autophagy flux during fasting-induced skeletal muscle atrophy

Derek W. Stouth^a, Tiffany L. vanLieshout^a, Andrew I. Mikhail^a, Sean Y. Ng^a, Rozhin Raziee^a, Brittany A. Edgett^b, Goutham Vasam^c, Erin K. Webb^a, Kevin S. Gilotra^a, Matthew Markou^a, Hannah C. Pineda^a, Brianna G. Bettencourt-Mora^a, Haleema Noor^a, Zachary Moll^a, Megan E. Bittner^a, Brendon J. Gurd^b, Keir J. Menzies^{c,d}, and Vladimir Ljubovic^{ib}^a

^aDepartment of Kinesiology, McMaster University, Hamilton, Ontario, Canada; ^bSchool of Kinesiology and Health Studies, Queen's University, Kingston, Ontario, Canada; ^cInterdisciplinary School of Health Sciences, Faculty of Health Sciences, University of Ottawa, Ottawa, Ontario, Canada; ^dOttawa Institute of Systems Biology and the Centre for Neuromuscular Disease, Department of Biochemistry, Microbiology and Immunology, Faculty of Medicine, University of Ottawa, Ottawa, Ontario, Canada

ABSTRACT

CARM1 (coactivator associated arginine methyltransferase 1) has recently emerged as a powerful regulator of skeletal muscle biology. However, the molecular mechanisms by which the methyltransferase remodels muscle remain to be fully understood. In this study, *carm1* skeletal muscle-specific knockout (mKO) mice exhibited lower muscle mass with dysregulated macroautophagic/autophagic and atrophic signaling, including depressed AMP-activated protein kinase (AMPK) site-specific phosphorylation of ULK1 (unc-51 like autophagy activating kinase 1; Ser555) and FOXO3 (forkhead box O3; Ser588), as well as MTOR (mechanistic target of rapamycin kinase)-induced inhibition of ULK1 (Ser757), along with AKT/protein kinase B site-specific suppression of FOXO1 (Ser256) and FOXO3 (Ser253). In addition to lower mitophagy and autophagy flux in skeletal muscle, *carm1* mKO led to increased mitochondrial PRKN/parkin accumulation, which suggests that CARM1 is required for basal mitochondrial turnover and autophagic clearance. *carm1* deletion also elicited PPARGC1A (PPARG coactivator 1 alpha) activity and a slower, more oxidative muscle phenotype. As such, these *carm1* mKO-evoked adaptations disrupted mitophagy and autophagy induction during food deprivation and collectively served to mitigate fasting-induced muscle atrophy. Furthermore, at the threshold of muscle atrophy during food deprivation experiments in humans, skeletal muscle CARM1 activity decreased similarly to our observations in mice, and was accompanied by site-specific activation of ULK1 (Ser757), highlighting the translational impact of the methyltransferase in human skeletal muscle. Taken together, our results indicate that CARM1 governs mitophagic, autophagic, and atrophic processes fundamental to the maintenance and remodeling of muscle mass. Targeting the enzyme may provide new therapeutic approaches for mitigating skeletal muscle atrophy.

Abbreviation: ADMA: asymmetric dimethylarginine; AKT/protein kinase B: AKT serine/threonine kinase; AMPK: AMP-activated protein kinase; ATG: autophagy related; BECN1: beclin 1; BNIP3: BCL2 interacting protein 3; CARM1: coactivator associated arginine methyltransferase 1; Col: colchicine; CSA: cross-sectional area; CTNS: cystinosin, lysosomal cystine transporter; EDL: extensor digitorum longus; FBXO32/MAFbx: F-box protein 32; FOXO: forkhead box O; GAST: gastrocnemius; H₂O₂: hydrogen peroxide; IMF: intermyofibrillar; LAMP1: lysosomal associated membrane protein 1; MAP1LC3B: microtubule associated protein 1 light chain 3 beta; mKO: skeletal muscle-specific knockout; MMA: monomethylarginine; MTOR: mechanistic target of rapamycin kinase; MYH: myosin heavy chain; NFE2L2/NRF2: NFE2 like bZIP transcription factor 2; OXPHOS: oxidative phosphorylation; PABPC1/PABP1: poly(A) binding protein cytoplasmic 1; PPARGC1A/PGC-1α: PPARG coactivator 1 alpha; PRKN/parkin: parkin RBR E3 ubiquitin protein ligase; PRMT: protein arginine methyltransferase; Sal: saline; SDMA: symmetric dimethylarginine; SIRT1: sirtuin 1; SKP2: S-phase kinase associated protein 2; SMARCC1/BAF155: SWI/SNF related, matrix associated, actin dependent regulator of chromatin subfamily c member 1; SOL: soleus; SQSTM1/p62: sequestosome 1; SS: subsarcolemmal; TA: tibialis anterior; TFAM: transcription factor A, mitochondrial; TFEb: transcription factor EB; TOMM20: translocase of outer mitochondrial membrane 20; TRIM63/MuRF1: tripartite motif containing 63; ULK1: unc-51 like autophagy activating kinase 1; VPS11: VPS11 core subunit of CORVET and HOPS complexes; WT: wild-type.

ARTICLE HISTORY

Received 17 January 2023
Revised 17 November 2023
Accepted 20 November 2023



KEYWORDS


Atrophy; autophagy; coactivator-associated arginine methyltransferase 1; fasting; mitophagy; skeletal muscle

Introduction

CARM1 (coactivator associated arginine methyltransferase 1), a member of the PRMT (protein arginine methyltransferase)

enzyme family, catalyzes the transfer of methyl groups to arginine residues on target proteins, thereby controlling the stability, localization, and/or activity of marked substrates [1–4]. As such,

CONTACT Vladimir Ljubovic  ljubicic@mcmaster.ca  Department of Kinesiology, McMaster University, Hamilton, Ontario L8S 4L8, Canada

 Supplemental data for this article can be accessed online at <https://doi.org/10.1080/15548627.2023.2288528>

© 2023 The Author(s). Published by Informa UK Limited, trading as Taylor & Francis Group.

This is an Open Access article distributed under the terms of the Creative Commons Attribution-NonCommercial-NoDerivatives License (<http://creativecommons.org/licenses/by-nc-nd/4.0/>), which permits non-commercial re-use, distribution, and reproduction in any medium, provided the original work is properly cited, and is not altered, transformed, or built upon in any way. The terms on which this article has been published allow the posting of the Accepted Manuscript in a repository by the author(s) or with their consent.

via arginine methylation CARM1 regulates diverse cellular processes such as signal transduction, DNA repair, transcriptional control, mRNA splicing, and cell cycle progression, among others. In fact, the occurrence of this post-translational modification is comparable to that of the essential and much more studied threonine/serine phosphorylation and lysine ubiquitination [5,6], which indicates that arginine methylation is a major mark that deserves further awareness and understanding. Given its importance, it is not surprising that CARM1 is ubiquitously expressed and whole-body genetic deletion of this methyltransferase results in perinatal lethality [7]. Thus, since CARM1 is required for survival, targeted approaches are needed when studying the enzyme.

Recent work from our laboratory [6,8–16] and others [17–23], demonstrate that CARM1 is emerging as a particularly important enzyme for the maintenance and remodeling of skeletal muscle biology. For example, the methyltransferase impacts skeletal muscle fiber type composition, mitochondrial morphology, and neuromuscular junction stability, and skeletal muscle-specific *carm1* deletion alters transcriptomic and arginine methylproteomic signatures, including changes related to muscle atrophy genes [6]. CARM1 influences the expression and function of the master neuromuscular phenotypic modifier AMPK (AMP-activated protein kinase) and its downstream signaling network to influence muscle mass and the progression of neurogenic disuse-evoked muscle atrophy [15]. CARM1 likely regulates skeletal muscle homeostasis and plasticity, at least in part, by influencing the autophagy-lysosome system [15,21]. For instance, transient knockdown of *Carm1* attenuates the expression of *Atg* (autophagy related) genes such as *Atg13* and *Atg14*, following neurogenic muscle disuse [21]. Skeletal muscle-specific deletion of *Carm1* also curtails phosphorylation of AMPK targets such as ULK1 (unc-51 like autophagy activating kinase 1) in response to denervation, which occurs coincident with blunted progression of muscle atrophy [15]. However, the role of CARM1 in regulating autophagy-lysosome biology in skeletal muscle remains to be fully understood. It is interesting to note here that Shin and colleagues previously demonstrated that CARM1 is at the nexus of a signaling cascade that governs macroautophagy/autophagy [24,25] and it is tempting to speculate that this is also the case in skeletal muscle, a tissue that is essential for respiration, metabolism, and mobility. Therefore, in the current study, we sought to elucidate the molecular mechanisms whereby CARM1 contributes to autophagic processes in skeletal muscle in vivo. We hypothesized that muscle-specific deletion of *Carm1* would hinder autophagic flux during periods of prolonged food deprivation and result in attenuated fasting-induced loss of muscle mass.

Results

Skeletal muscle-specific deletion of *carm1* attenuates progression of fasting-induced atrophy.

We previously generated *carm1* mKO (skeletal muscle-specific knockout) mice to investigate the function of CARM1 during neurogenic muscle disuse [15]. Similar to a transient knockdown approach [21], knockout of *Carm1* in muscle

blunted denervation-induced muscle wasting [15]. Since the impact of CARM1 on muscle wasting during food deprivation remains unclear, we sought to employ mKO animals to study the role of CARM1 during fasting-induced muscle atrophy. We selected food deprivation as an atrophy model since the autophagy-lysosome and ubiquitin-proteasome systems are rapidly and robustly activated [26]. Prolonged fasting also elicits dramatic changes to the mitochondrial network [27]. Immunoblot analysis confirmed deletion of *Carm1* in skeletal muscle (Figure 1A). Compared to fed conditions, CARM1 protein and mRNA expression levels were similar in the TA (tibialis anterior) and EDL (extensor digitorum longus) muscles, respectively, following 24 and 48 h of food deprivation (Figure 1A,B and Figure S1A). *Carm1* transcript levels were significantly elevated by 2-fold after 24 h of fasting in the SOL (soleus) muscle (Figure S1B).

Body mass was 5% lower ($p < 0.05$) in mKO versus wild-type (WT) mice under fed conditions (Figure 1C). Food deprivation induced a significant ~10% and ~20% decrease in body mass after 24 and 48 h, respectively, in both genotypes relative to their respective fed littermates. The relative decline in body mass between fed and 48 h fasted conditions trended lower in mKO versus WT animals ($p = 0.06$). When compared to WT fed animals, TA muscle mass was significantly reduced by ~15% in WT mice after 48 h of fasting (Figure 1D). No significant changes in TA muscle mass were detected in mKO animals under fed versus fasting conditions. Relative to the WT fed group, quadriceps (QUAD) and gastrocnemius (GAST) muscle mass decreased by 20% ($p < 0.05$) in WT animals after 48 h of food deprivation. GAST muscle mass was also significantly lower by 20% in mKO versus WT mice under fed settings. Moreover, QUAD and GAST muscle mass did not differ between fed and fasted mKO animals. EDL and SOL muscle mass significantly decreased in both genotypes after fasting (Figure S1C, D). Relative to the WT fed group, food deprivation elicited a ~30% decrease ($p < 0.05$) in EDL cross-sectional area (CSA) after 48 h, which was not observed in the absence of CARM1 (Figure 1E,F). There was a significant decrease in SOL myofiber CSA in both groups after fasting (Figure S1E, F).

We recently uncovered a distinct muscle atrophy gene signature in mKO mice compared to WT animals under fed conditions [6]. Here, of the 277 downregulated genes in mKO versus WT muscle, 161 were correlated with biosets of skeletal muscle atrophy. From the 206 upregulated genes in mKO versus WT mice, 98 were correlated with muscle atrophy. In the current study, we sought to compare global transcriptional changes in mKO versus WT mice in response to 48 h of fasting using RNA-seq analysis of TA muscles. We found 881 and 639 commonly downregulated and upregulated genes, respectively, in both genotypes after 48 h of fasting (Figure 1G). In response to food deprivation, there were 545 and 636 uniquely downregulated and upregulated genes, respectively, in WT versus mKO mice. Compared to WT mice, there were 894 and 1,393 uniquely downregulated and upregulated genes, respectively, in mKO animals after fasting. We next carried out principal component (PC) analysis of transcript abundances. Sample coordinates on the first two PCs revealed a transition from fed to fast phases, with

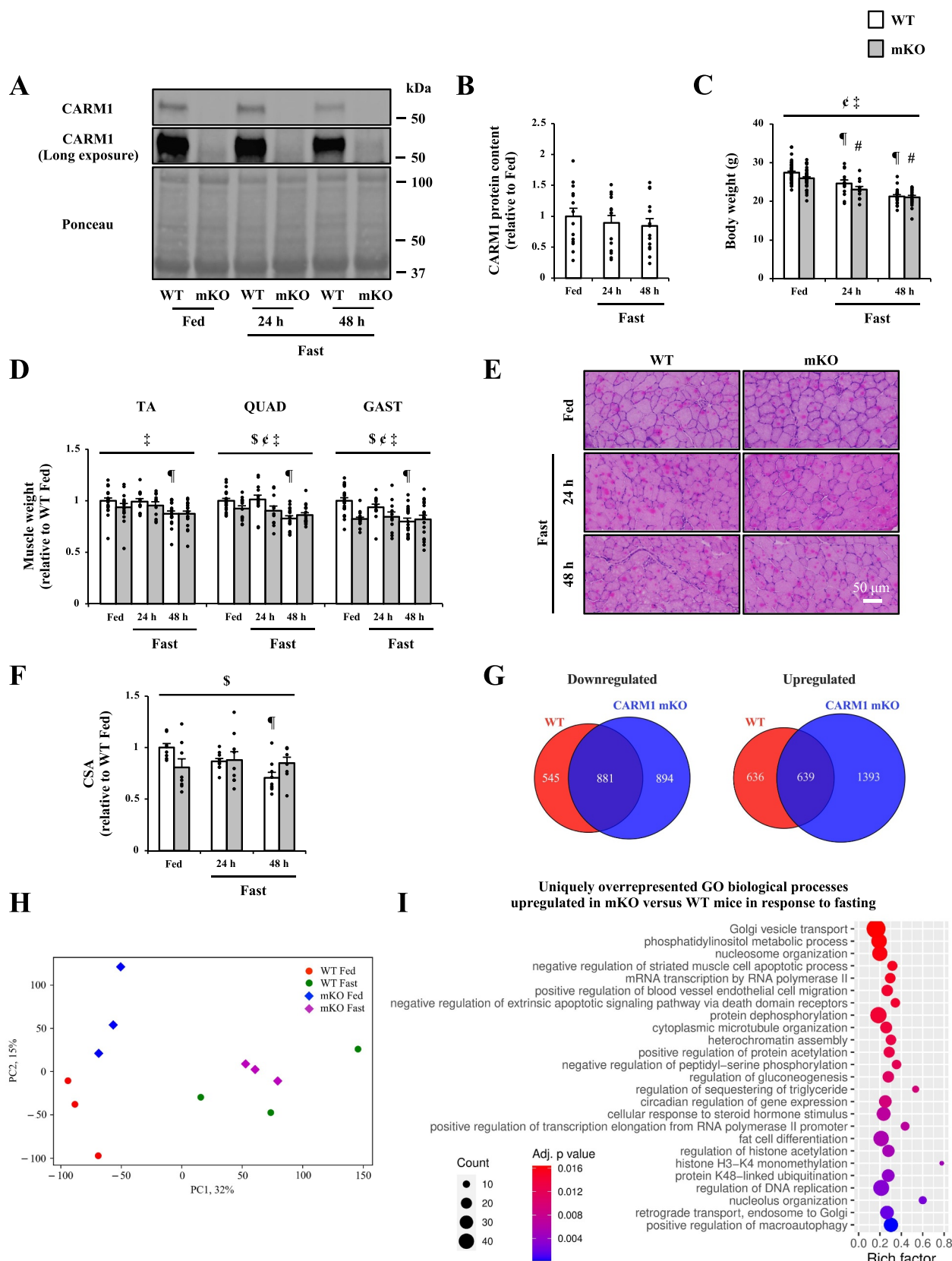


Figure 1. Fasting-induced atrophy in *carm1* mKO (skeletal muscle-specific knockout) mice. (A) Representative western blots of CARM1 protein content (normal and long exposures) in the TA (tibialis anterior) muscle from WT (wild-type) and mKO mice under fed and fast (24 and 48 h) conditions, as well as a representative Ponceau stain, below. Molecular masses (kDa) are shown at right of blots. (B) Graphical summary of CARM1 protein expression in TA muscle of WT animals. Data are expressed as protein content relative to fed ($n = 14$). (C) Body mass of WT and mKO animals in response to fasting ($n = 11$ – 21). (D) TA, quadriceps (QUAD), and gastrocnemius (GAST) muscle mass from WT and mKO mice in fed and fast conditions. Muscle weight data are expressed relative to WT fed ($n = 11$ – 21). (E) Representative images of hematoxylin and eosin (H&E)-stained EDL muscle cross sections from WT and mKO mice in fed and fast cohorts. Scale bar: 50 μ m. (F) Graphical summary of the average myofiber cross-sectional area (CSA) of EDL muscles from WT and mKO mice in response to fasting. Data are expressed as CSA relative to the WT fed ($n = 8$ – 9). Data are means \pm SEM. Two-way ANOVA; $\$$ $p < 0.05$ interaction effect of genotype and fasting; ζ $p < 0.05$ main effect of genotype; \ddagger

moderate genotype-based clustering (Figure 1H). Notably, several upregulated Gene Ontology (GO) biological processes, including positive regulation of macroautophagy (GO:0016239), regulation of muscle hypertrophy (GO:0014743), and positive regulation of protein localization to nucleus (GO:1900182) were uniquely overrepresented in mKO versus WT mice in response to 48 h of fasting (Figure 1I and data not shown).

PRMT content and activity in mKO mice after food deprivation

We desired to determine whether knocking out *Carm1* in muscle evoked changes in other PRMTs in response to fasting. We initially performed transcriptomic analyses of all PRMTs by RNA sequencing TA muscles from WT and mKO animals under fed and 48 h fasted conditions. CARM1 had minor effects on global *Prmt* transcription after fasting (Figure 2A). We sought to extend these data with gene expression analyses in EDL and SOL muscles, plus protein content in TA muscles for PRMT1, PRMT5, PRMT6, and PRMT7 in WT and mKO animals following 24 and 48 h of food deprivation. We observed a significant decrease in *Prmt6* mRNA content in both genotypes in the EDL after fasting (Figure 2B). In contrast, *Prmt1*, *Prmt5*, and *Prmt7* transcript levels were similar in the EDL muscle between all experimental conditions. There was a significant increase in *Prmt1* and *Prmt5* mRNA content in WT and mKO SOL muscles in response to food deprivation (Figure S2A). *Prmt7* transcript levels were greater ($p < 0.05$) in mKO versus WT SOL muscle. Furthermore, we observed a significant increase in PRMT1 protein content in WT and mKO TA muscles after fasting (Figure 2C,D). PRMT1 and PRMT7 protein levels were greater ($p < 0.05$) in mKO versus WT animals, whereas PRMT6 protein content was lower ($p < 0.05$) in mKO versus WT mice. PRMT5 protein expression was similar in all experimental conditions.

We next examined markers of global type I and type II PRMT activities, such as monomethylarginine (MMA), asymmetric dimethylarginine (ADMA), and symmetric dimethylarginine (SDMA) content [1,2]. We also measured asymmetric arginine dimethylation of pan-CARM1-marked substrates [28,29], as well as bona fide CARM1 targets SMARCC1/BAF155 (SWI/SNF related, matrix associated, actin dependent regulator of chromatin, subfamily c, member 1) me2a (Arg1064) and PABPC1/PABP1 (poly(A) binding protein, cytoplasmic 1) me2a (Arg455/Arg460). Relative to the WT fed group, *carm1* deletion resulted in a significant ~45% decrease in CARM1 substrate arginine methylation levels under fed and fasted settings (Figure 2C,E). MMA, ADMA, and SDMA content were similar between genotypes with food deprivation. Food deprivation induced a 40% decrease ($p < 0.05$) in SMARCC1 me2a (Arg1064) in WT mice after 48 h relative to their WT fed littermates (Figure 2C,F). Compared

to WT fed mice, SMARCC1 me2a (Arg1064) was significantly lower by ~70% in fed and fasted mKO animals. Total SMARCC1 protein content was similar between all groups. Compared to WT animals, SMARCC1 methylation status (i.e., the methylated form of the protein relative to its total, unmethylated content) was lower ($p < 0.05$) in mKO mice. Relative to WT fed mice, PABPC1 me2a (Arg455/Arg460) significantly decreased by ~50% in WT animals in response to 24 and 48 h of food deprivation (Figure 2C,G). PABPC1 me2a (Arg455/Arg460) was also lower ($p < 0.05$) by ~65% in fed and fasted mKO muscle versus fed WT mice. Similar levels of PABPC1 me2a (Arg455/Arg460) in mKO animals between fed and fasted muscle were observed. There was a significant decrease in total PABPC1 protein content in both genotypes after fasting. Compared to the WT fed group, PABPC1 methylation status was significantly lower by 60% in mKO mice during fed and fasted conditions.

The impact of *carm1* mKO on metabolic signaling during fasting-induced muscle wasting

Previous work has shown that *carm1* deletion in muscle affects the expression and/or activity of molecules involved in metabolic signaling during neurogenic muscle disuse [15]. We wished to determine whether CARM1 was important for metabolic signaling in response to food deprivation. As such, we first assessed the transcript levels of important mitochondrial genes such as *Sirt1* (sirtuin 1), *Ppargc1a/Pgc-1α* (PPARG coactivator 1 alpha), *Tfam* (transcription factor A, mitochondrial), *Cox4* (cytochrome c oxidase subunit 4), and *Nfe2l2/Nrf2* (NFE2 like bZIP transcription factor 2) in EDL and SOL muscles from fed and fasted WT and mKO mice. *Sirt1*, *Ppargc1a*, *Tfam*, *Cox4*, and *Nfe2l2* mRNA content was greater in mKO versus WT EDL muscle during fed and fasted conditions (Figure S3A). *Nfe2l2* transcript levels were elevated ($p < 0.05$) in both genotypes with fasting in the EDL. Furthermore, *Sirt1*, *Ppargc1a*, *Tfam*, *Cox4*, and *Nfe2l2* mRNA content was significantly increased in WT and mKO SOL muscles following food deprivation (Figure S3B). We next sought to determine whether a known target of *Ppargc1a* mRNA processing activity *Ndr4* (NDRG family member 4) [30], was affected by *carm1* deletion in muscle. We observed elevated ($p < 0.05$) PPARGC1A activity in mKO versus WT mice, as indicated by increased alternative splicing of *Ndr4*, in EDL and SOL muscle (Figure S3A, B).

We next examined the phosphorylation status of AMPK, as well as protein content of PPARGC1A, CS (citrate synthase), and proteins indicative of mitochondrial oxidative phosphorylation (OXPHOS) complexes I – V (CI – CV). Compared to the WT fed group, phosphorylated (p)-PRKKA/AMPK (Thr172) content was significantly greater by 4–5-fold in WT animals after 24 and 48 h of food deprivation, whereas

$p < 0.05$ main effect of fasting; ¶ $p < 0.05$ versus WT fed; # $p < 0.05$ versus mKO fed. (G) venn diagram representation of the number of significantly down- and upregulated genes in the TA muscle from WT and mKO mice based on RNA-seq following 48 h fast ($n = 3$). (H) Principal component (PC) analysis of transcript abundances in WT and mKO mice under fed and fast conditions ($n = 3$). (I) bubble plot of top 25 uniquely overrepresented gene ontology (GO) biological processes upregulated in mKO versus WT mice following 48 h fast ($n = 3$).

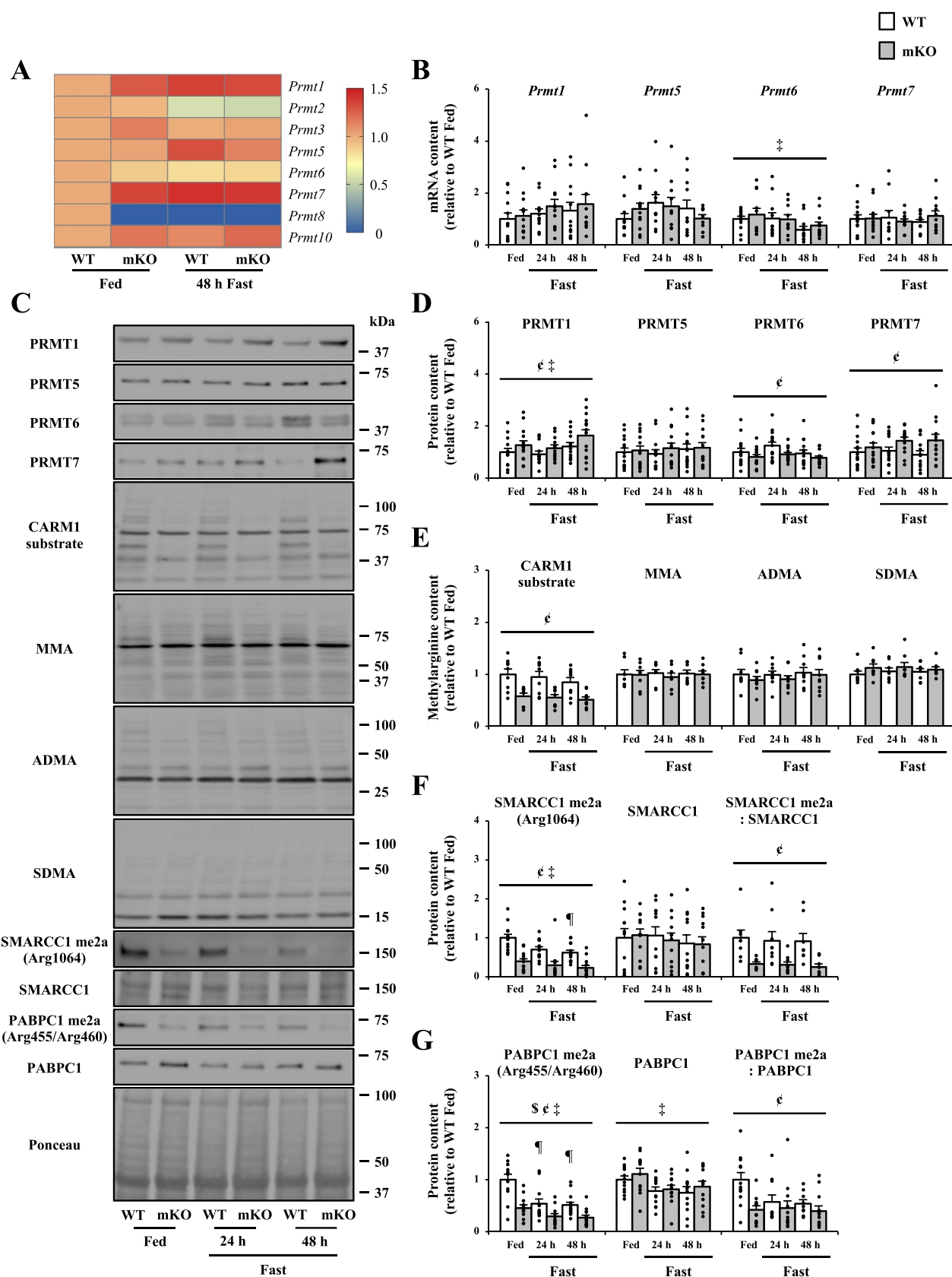


Figure 2. PRMT (protein arginine methyltransferase) content and activity in mKO animals following fasting-evoked muscle wasting. (A) heatmap of PRMT family members in TA muscle of WT and mKO mice after fasting. Data are expressed relative to WT fed ($n = 3$). (B) PRMT1, PRMT5, PRMT6, and PRMT7 mRNA expression in EDL muscles from WT and mKO mice during fed and fast conditions. Data are expressed as mRNA content relative to WT fed muscle ($n = 9-13$). (C) typical western blots of PRMT1, PRMT5, PRMT6, PRMT7, monomethylarginine (MMA), asymmetric dimethylarginine (ADMA), asymmetric arginine dimethylated CARM1 substrates, symmetric dimethylarginine (SDMA), asymmetrically dimethylated SMARCC1/BAF155 (SWI/SNF related, matrix associated, actin dependent regulator of chromatin, subfamily c, member 1) me2a (Arg1064), total SMARCC1, asymmetrically dimethylated PABPC1/PABP1 (poly(A) binding protein, cytoplasmic 1) me2a (Arg455/Arg460), and total PABPC1 in TA muscles from WT and mKO animals in fed and fast cohorts, accompanied by a typical Ponceau stain. Molecular masses (kDa) are shown at the right of blots. (D-G) graphical summaries of PRMT1, PRMT5, PRMT6, PRMT7, MMA, ADMA, CARM1 substrate, SDMA, SMARCC1 me2a (Arg1064),

p-PRKAA (Thr172) was similar between fed and fasted conditions in mKO mice (Figure 3A,B). Total AMPK was greater ($p < 0.05$) in mKO versus WT muscle during fed and fasted conditions. Relative to the WT fed group, AMPK phosphorylation status was significantly greater by ~6-fold in WT animals following 24 and 48 h of food deprivation, whereas AMPK phosphorylation status did not change between fed and fasted conditions in mKO mice. After 48 h of food deprivation, PPARGC1A protein expression was significantly greater by ~2-fold in mKO mice compared to the fed mKO group (Figure 3A,C). CS protein content was significantly increased in both genotypes after fasting, whereas total OXPHOS expression was similar between conditions.

We sought to investigate the fiber type composition of WT and mKO EDL muscles in response to food deprivation (Figure 3D,E). Under fed and fasted conditions, MYH (myosin heavy chain) type IIA was greater in mKO versus WT mice, whereas MYH type IIB was lower in mKO versus WT animals. MYH type I and MYH type IIX were similar in all experimental conditions. To gain further insight into the effects of *carm1* deficiency on mitochondria structure, we next conducted transmission electron microscopy analysis (Figure 3F,G). Mitochondria size was similar in all experimental conditions, regardless of SS (subsarcolemmal) or IMF (intermyofibrillar) location (Figure S3C). In the SS region, mitochondria per unit area decreased by 50% in WT animals after 48 h of fasting ($p = 0.06$), whereas mitochondria per unit area was similar between fed and fasted conditions in mKO mice. Furthermore, an interaction ($p = 0.08$) between genotype and fasting was observed in the IMF section (Figure S3D). A solid trend toward an interaction between genotype and fasting emerged for IMF ($p = 0.07$) and total ($p = 0.09$) mitochondria density (Figure 3F,H).

Given the impact of CARM1 on metabolic signaling, we performed analyses of SDH (succinate dehydrogenase) content, along with mitochondrial respiration and hydrogen peroxide (H_2O_2) emission. After 48 h of food deprivation, SDH staining intensity was significantly greater by 1.2-fold in mKO animals compared to the fed mKO group (Figure 3I,J). When normalized to muscle fiber bundle weight, complex I (CI)-supported state III respiration and CI + II-supported state III respiration, was greater in mKO versus WT mice under fed and fasted conditions (Figure 3K,L). CI-supported state III H_2O_2 emission was elevated in WT and mKO animals after 48 h of fasting (Figure S3E).

Mitophagy in mKO animals following food deprivation.

To determine mitophagy flux, WT and mKO mice were treated with saline or colchicine under fed and fasted conditions. Mitochondria were then isolated from QUAD muscles, followed by western blotting of LC3 (microtubule-associated protein 1A/1B-light chain 3)-II and SQSTM1/p62 (sequestosome 1). We observed main effects ($p < 0.05$) of genotype and

fasting for LC3-II and SQSTM1 flux (Figure 4A–C). Transmission electron microscopy was used to assess the accumulation of abnormal mitochondria (Figure 4D) in WT and mKO animals under saline or colchicine-treated conditions in both fed and fasted muscle. Abnormal mitochondria were defined as organelles with disrupted membranes, loss of cristae, and vacuolization [31]. Colchicine increased the total number of abnormal mitochondria in both genotypes under fasted settings (Figure 4D,E).

We next examined the mitophagy protein PRKN/parkin (parkin RBR E3 ubiquitin protein ligase) in mitochondria isolated from QUAD muscles of WT and mKO animals following fasting. An interaction ($p < 0.05$) between genotype and fasting on mitochondrial PRKN content was detected (Figure 4F,G). To complement this analysis, EDL myofiber cross-sections were stained for PRKN and TOMM20 (translocase of outer mitochondrial membrane 20) in WT and mKO mice during food deprivation (Figure 4H). Relative to the WT fed group, fasting induced a significant 1.8-fold increase in PRKN puncta following 24 and 48 h in WT mice (Figure 4I). In contrast, the number of PRKN puncta was similar between fed and fasted mKO animals.

We further investigated the impact of *carm1* mKO on genes that regulate mitophagy. In particular, we assessed *Prkn* and *Bnip3* (BCL2 interacting protein 3) transcript levels in EDL and SOL muscles from fed and fasted WT and mKO mice. *Prkn* and *Bnip3* mRNA content was significantly elevated in both genotypes in EDL and SOL muscles (Figure 4J and Figure S4A). When compared to the WT fed group, PRKN protein content increased by 2-fold ($p < 0.05$) in WT animals after 24 h of food deprivation (Figure 4K,L). PRKN protein expression was also significantly greater by 1.7-fold in mKO versus WT muscle under fed conditions. Similar PRKN protein levels between fed and fasted mKO mice were observed. BNIP3 protein expression significantly increased by 2.5-fold in WT muscle following 48 h of food deprivation compared to their fed WT littermates. BNIP3 protein content was greater by 3-fold ($p < 0.05$) in mKO muscle after 48 h of fasting relative to the fed mKO animals. The relative increase in BNIP3 protein expression between fed and 48 h fasted groups trended larger in mKO versus WT mice ($p = 0.08$).

Autophagy in mKO mice in response to fasting

Previous studies have shown that CARM1 regulates the autophagic process in non-muscle cells in response to nutrient deprivation [24]. Here, we sought to determine whether CARM1 governs myofiber autophagy. To this end, we administered saline or colchicine to WT and mKO mice under fed and fasted conditions to evaluate autophagosome turnover in whole TA muscle (Figure 5A). We noted significant main effects of genotype and fasting on LC3-II and SQSTM1 flux (Figure 5A–C). Transmission electron microscopy was

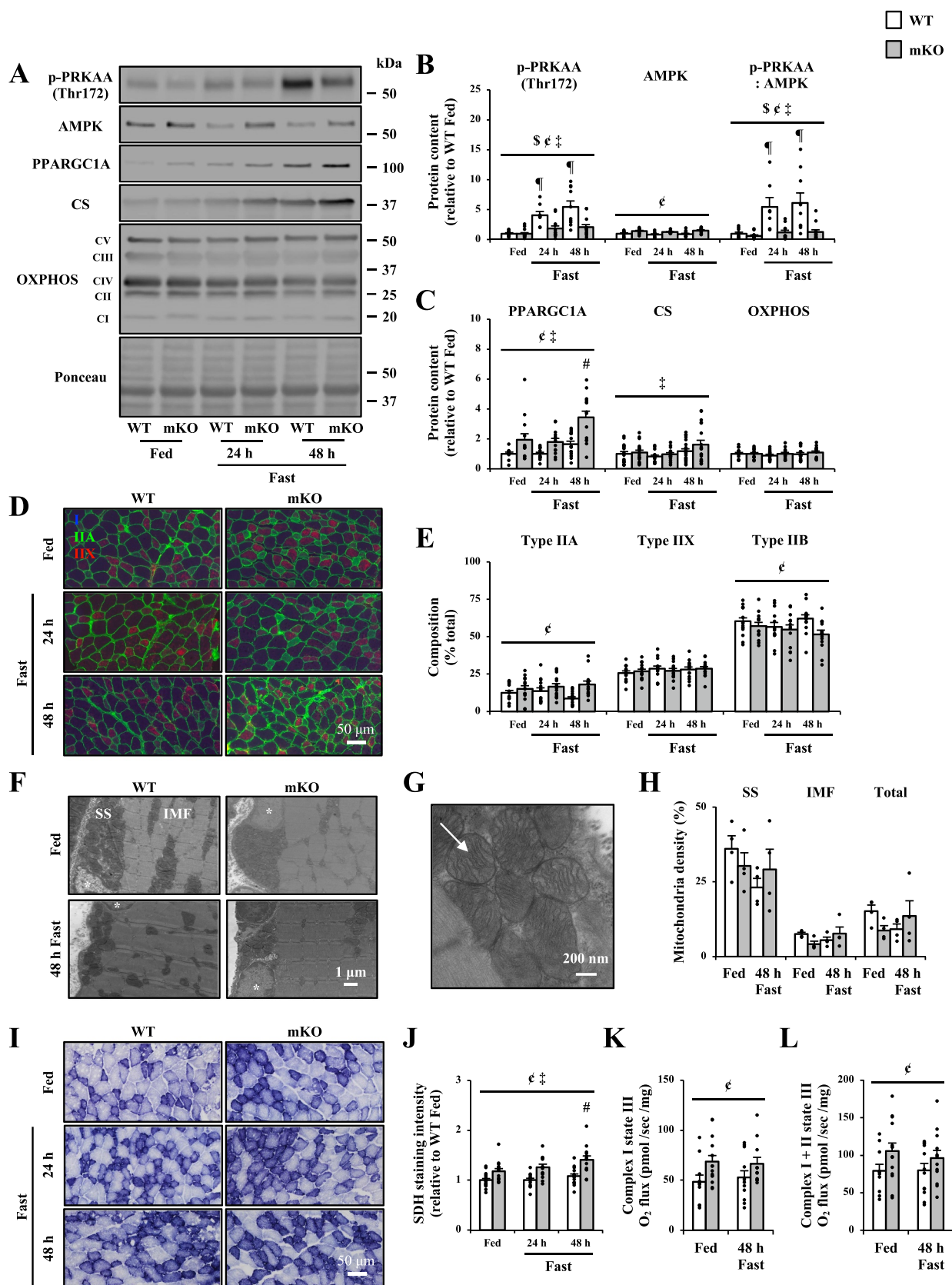


Figure 3. CARM1 regulates metabolic signaling during fasting-induced muscle atrophy. (A) Representative western blots of phosphorylated AMP-activated protein kinase (p-PRKAA/AMPK [Thr172]), total AMPK, PPARGC1A/PGC-1 α (PPARG coactivator 1 alpha), CS (citrate synthase), and proteins indicative of mitochondrial OXPHOS (oxidative phosphorylation) complexes I – V (CI – CV) in WT and mKO TA muscles following fasting, accompanied by a typical Ponceau stain. Molecular masses (kDa) are shown at the right of blots. (B–C) graphical summaries of p-PRKAA/AMPK (Thr172), AMPK, AMPK phosphorylation status, PPARGC1A, CS, and total OXPHOS protein expression in WT and mKO TA muscles in response to fasting. Data are expressed as protein content relative to WT fed ($n = 8–21$). (D) Representative immunofluorescence images of MYH (myosin heavy chain) type I (blue), IIA (green), IIX (red), and IIB (black) in EDL muscles of WT and mKO mice after fasting. (E) graphical summaries of EDL myofiber MYH composition in both genotypes following food deprivation. (F) typical transmission electron micrographs of mitochondria and myonuclei (*) within the SS (sarsarcolemmal) and IMF (intermyofibrillar) regions of TA muscle in WT and mKO mice under fed and 48 h fast conditions. Scale bar:

employed to evaluate the accumulation of autophagic vacuoles (Figure 5D) in WT and mKO mice under saline or colchicine-treated conditions in both fed and fasted muscle. Colchicine increased the total number of autophagic vacuoles in WT and mKO animals during food deprivation (Figure 5D,E).

We identified upregulated autophagy genes from our RNA-seq analysis that were uniquely overrepresented in mKO versus WT muscle in response to 48 h of fasting. For example, the enrichment of *Ulk1*, *Smcr8*, *Wipi1*, *Tbk1*, *Wdr45*, *Supt5*, *Ambra1*, *Pip4k2c*, *Optn*, and *Epm2a* were unique to *carm1* mKO TA muscle during food deprivation (Figure 5F). We also investigated autophagy-related and lysosomal genes previously demonstrated to be transcriptionally regulated by CARM1 in non-muscle cells [24]. *Map1lc3b*, *Atg12*, *Atg14*, *Vps11*, and *Ctns* transcript levels were significantly elevated in both genotypes after fasting (Figure S5A, B). To further understand the role of CARM1 in regulating myofiber autophagy, we also probed for autophagy-related *Becn1* (beclin 1), *Gabarapl1*, and lysosomal *Ctsl* mRNA content in EDL and SOL muscles. Compared to WT mice, *Becn1* mRNA expression in the EDL was significantly greater in mKO animals under fed and fasted settings. *Gabarapl1* and *Ctsl* transcript levels were elevated ($p < 0.05$) in both genotypes following food deprivation (Figure S5A, B).

We continued to evaluate the autophagy-lysosome pathway by assessing the phosphorylation status of ATG16L1, MTOR (mechanistic target of rapamycin kinase), ULK1, as well as the protein expression of TFEB (transcription factor EB), SKP2 (S-phase kinase associated protein 2), BECN1, LAMP1 (lysosomal associated membrane protein 1), LAMP2, and CTSD (cathepsin D). p-ATG16L1 (Ser278) was significantly lower in mKO versus WT animals under fed and fasted conditions (Figure 5G,H). Total ATG16L1 protein content was similar between genotypes with food deprivation. Relative to the WT fed group, ATG16L1 phosphorylation status was significantly greater by ~2-fold in WT animals following 24 h of food deprivation, whereas ATG16L1 phosphorylation status did not change between fed and fasted conditions in mKO mice. Moreover, qualitative analyses suggest that the relative increase in p-ATG16L1 (Ser278) puncta between fed and 24 h fasted conditions was lower in mKO versus WT animals (Figure 5I). Compared to WT animals, p-MTOR (Ser2448) and total MTOR was greater in mKO mice under fed and fasted settings (Figure 5G,J). Furthermore, MTOR phosphorylation status was similar between genotypes with food deprivation. Relative to the WT fed group, food deprivation evoked a significant 1.5-fold increase in p-ULK1 (Ser555) after 48 h in WT mice (Figure 5G,K). In contrast, similar p-ULK1 (Ser555) levels were detected between fed and fasted mKO animals. p-ULK1 (Ser757) levels were larger ($p < 0.05$) in mKO versus WT mice under fed and fasted settings. Total ULK1 protein content was significantly greater in both genotypes after fasting. Furthermore, TFEB protein expression was similar

between all groups (Figure 5G,L). When compared to the WT fed group, SKP2 protein content was significantly reduced by ~40% in fed and fasted mKO muscle. BECN1, LAMP1, and LAMP2 protein expression levels were greater ($p < 0.05$) in mKO versus WT animals under fed and fasted conditions. CTSD protein content was also significantly increased in both genotypes after fasting (data not shown).

The effects of CARM1 on muscle atrophy signaling during food deprivation

To probe the effect of *carm1* mKO on the muscle atrophy program during fasting, we screened pathways that are important for muscle wasting using RNA-seq analysis of TA muscles. Reactome pathway analysis of our RNA-sequencing results revealed upregulated pathways related to AKT/protein kinase B (AKT serine/threonine kinase) signaling that were uniquely overrepresented in mKO mice compared to WT animals in response to food deprivation (Figure 6A). Noteworthy reactome pathways influenced by *carm1* mKO included AKT phosphorylates targets in the cytosol (R-MMU-198323), regulation of FOXO (forkhead box O) transcriptional activity by acetylation (R-MMU-9617629), AKT-mediated inactivation of FOXO1A (R-MMU-211163), and AKT phosphorylates targets in the nucleus (R-MMU-198693). The enrichment of *Akt1*, *Akt2*, *Akt3*, *Foxo1*, and *Foxo3* genes were unique to *carm1* mKO compared to WT muscle in response to 48 h of fasting (Figure 6B).

We desired to further investigate the upstream signaling molecule AKT and its downstream targets FOXO1 and FOXO3. Compared to WT animals, p-AKT (Ser473) and total AKT were greater ($p < 0.05$) in mKO mice under fed and fasted settings (Figure 6C,D). Relative to the WT fed group, p-FOXO1 (Ser256) content was significantly reduced by 50% in WT animals after 48 h of food deprivation (Figure 6C,E). In contrast, p-FOXO1 (Ser256) did not change between fed and fasted conditions in mKO mice. FOXO1 phosphorylation status was ~60% lower ($p < 0.05$) in WT and mKO animals following 48 h of fasting versus their respective fed littermates. Compared to the WT fed group, food deprivation evoked a significant 40% decrease in p-FOXO3 (Ser253) in WT muscle following 24 and 48 h (Figure 6C,F). In contrast, levels of p-FOXO3 (Ser253) in mKO animals were similar between fed and fasted muscle. Moreover, we analyzed the phosphorylation status of AMPK downstream targets FOXO3 (Ser413) and FOXO3 (Ser588) [32], as CARM1 and AMPK coregulate autophagic and atrophic signaling [15,24,33,34]. Relative to the WT fed group, *carm1* deletion resulted in a significant 1.6-fold increase in p-FOXO3 (Ser413) levels under fed and fasted conditions. p-FOXO3 (Ser588) levels were lower ($p < 0.05$) in mKO versus WT mice during fed and fasted settings.

1 μm ($n = 4$). (G) Representative image from WT muscle of normal mitochondrial ultrastructure with intact membranes and clearly defined cristae (white arrow). Scale bar: 200 nm. (H) Transmission electron micrographs were analyzed for mitochondrial density ($\mu\text{m}^2 \times \#$ per $\mu\text{m}^2 \times 100$) within the SS and IMF areas of the muscle. (I) Representative images of succinate dehydrogenase (SDH)-stained EDL muscle cross-sections from WT and mKO mice after food deprivation. Scale bar: 50 μm ($n = 5-6$). (J) Graphical summary of SDH staining intensity in both genotypes following fasting. (K-L) complex I-supported state III respiration and complex I + II-supported state III respiration in WT and mKO TA muscle under fed and 48 h fast conditions ($n = 11-14$). Data are means \pm SEM. Two-way ANOVA; $\$ p < 0.05$ interaction effect of genotype and fasting; $\text{¢ } p < 0.05$ main effect of genotype; $\text{‡ } p < 0.05$ main effect of fasting; $\text{¶ } p < 0.05$ versus WT fed; $\text{\# } p < 0.05$ versus mKO Fed.

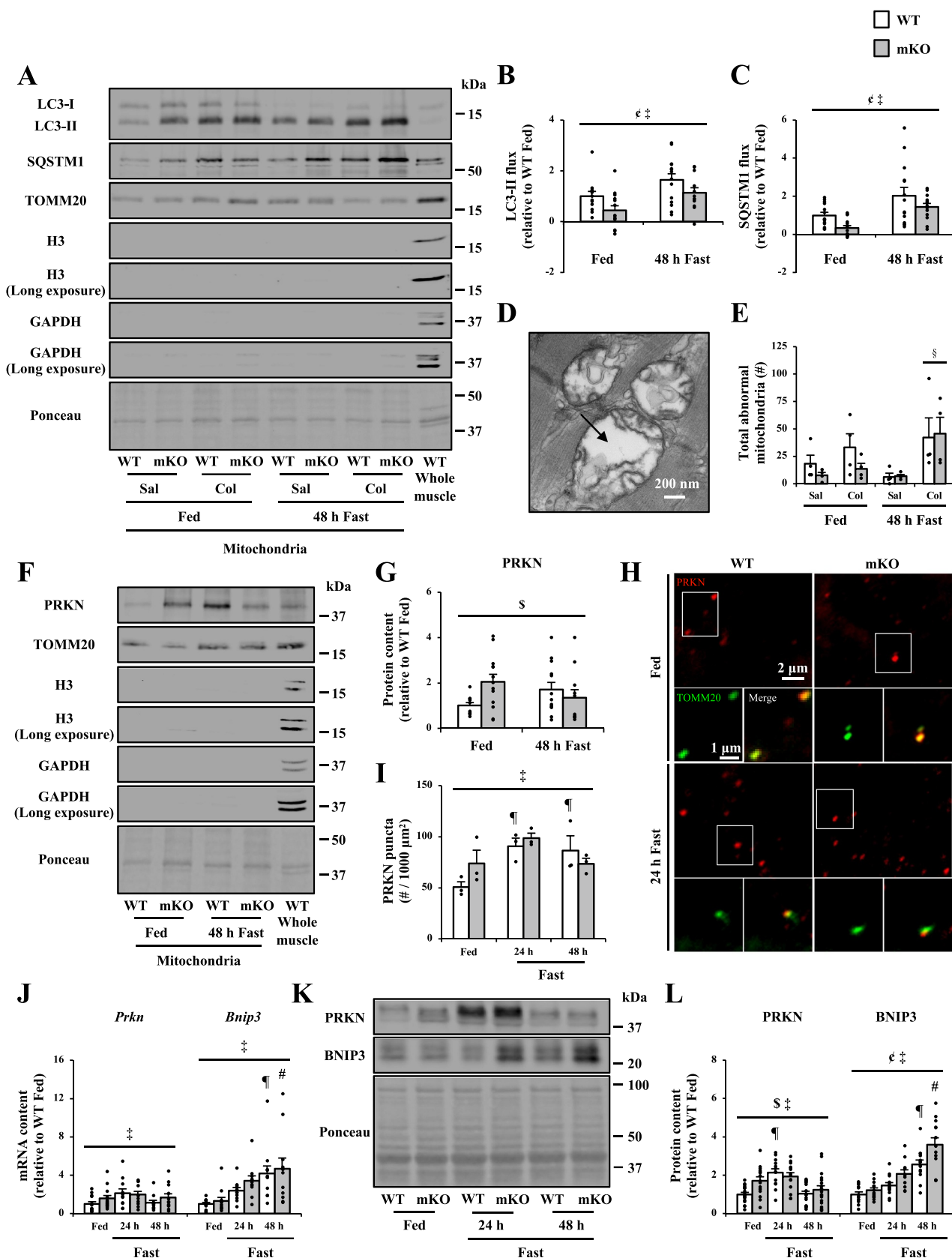


Figure 4. Mitophagy in mKO mice during fasting-evoked muscle atrophy. (A) Representative western blots of MAP1LC3/LC3 (microtubule associated protein 1 light chain 3)-I, LC3-II, SQSTM1, TOMM20 (translocase of outer mitochondrial membrane 20), histone H3 (normal and long exposures), and GAPDH (glyceraldehyde-3-phosphate dehydrogenase; normal and long exposures) in mitochondria isolated from QUAD muscles of WT and mKO mice treated with Sal (saline) or Col (colchicine) under fed and 48 h fast conditions. Blots are accompanied by a typical Ponceau stain. Molecular masses (kDa) are shown at the right of blots. (B-C) Graphical summaries of mitochondrial LC3-II and SQSTM1 flux in WT and mKO animals under fed and 48 h fast conditions. Data are expressed as protein content relative to WT fed ($n = 12-14$). (D) Representative image from mKO muscle of abnormal mitochondrial ultrastructure (black arrow) with disrupted membranes, loss of cristae, and vacuolization. (E) Graphical summary of total number of abnormal mitochondria in WT and mKO mice treated with Sal or Col under fed and 48 h fast conditions. (F) Representative western blots of PRKN/parkin (parkin RBR E3 ubiquitin protein ligase), TOMM20, histone H3 (normal and long exposures), and GAPDH

We complemented these data by assessing *Akt*, *Foxo1*, *Foxo3*, *Trim63/MuRF1* (tripartite motif containing 63) and *Fbxo32/MAFbx* (F-box protein 32) transcript levels in EDL muscles. We observed elevated ($p < 0.05$) *Akt*, *Foxo1*, *Foxo3*, *Trim63*, and *Fbxo32* mRNA content after fasting in WT and mKO animals (Figure S6A). Following 48 h of food deprivation, *Akt* mRNA expression was significantly increased by ~3-fold in mKO mice compared to the fed mKO group. *Foxo1* and *Foxo3* mRNA content was greater ($p < 0.05$) in mKO versus WT animals. TRIM63, FBXO32, and ubiquitin protein content was also significantly elevated after fasting (Figure S6B, C). For instance, TRIM63 protein expression was higher ($p < 0.05$) by ~4-fold in both genotypes after 24 and 48 h of food deprivation compared to their respective fed control group. Compared to the WT fed group, FBXO32 protein expression was significantly increased by 1.8-fold in WT animals following 24 and 48 h of fasting, whereas FBXO32 protein content was similar between fed and fasted conditions in mKO mice.

Myonuclear localization of muscle remodeling proteins during fasting-induced atrophy.

We evaluated myonuclear levels of CARM1, PRMT1, PRMT5, PRMT6, and PRMT7 in WT and mKO GAST muscle to further define their expression during atrophy elicited by food deprivation. We also analyzed the nuclear content of PPARGC1A, AMPK, FOXO1, FOXO3, and TFEB to more comprehensively understand how CARM1 governs myonuclear adaptations to fasting. Compared to fed conditions, nuclear CARM1 protein expression was significantly lower by ~30% in WT muscle after 48 h of food deprivation (Figure S6D, E). Nuclear PRMT1 protein content was similar between genotypes with food deprivation. Relative to the WT fed group, fasting induced a significant 40% decrease in nuclear PRMT5 protein expression in WT animals following 48 h of food deprivation, whereas no changes were detected in mKO animals. Compared to WT animals, we noted lower ($p < 0.05$) nuclear PRMT6 protein content in mKO mice. PRMT6 levels in myonuclei were significantly lower by ~50% in fed and fasted mKO muscle versus fed WT mice. Nuclear PRMT6 protein expression decreased by ~30% in WT mice following 48 h of food deprivation, whereas PRMT6 did not change between fed and fasted conditions in mKO animals. Interestingly, we did not detect PRMT6 in cytosolic fractions, whereas conversely, PRMT7 was excluded from myonuclei and found only in the cytosolic compartment (data not shown).

Main effects ($p < 0.05$) of genotype and fasting on nuclear PPARGC1A protein expression were observed (Figure S6D, F). When compared to the WT fed group, myonuclear p-PRKAA/AMPK (Thr172) increased by 5-fold ($p < 0.05$) in WT animals after 48 h of food deprivation. In contrast, nuclear p-PRKAA/AMPK (Thr172) did not significantly change between fed and fasted mKO mice. Nuclear AMPK phosphorylation status increased by 7-fold in WT animals following 48 h of food deprivation, whereas no significant changes were detected in mKO mice.

Relative to the WT fed group, total nuclear FOXO1 protein expression was elevated by 3-fold ($p < 0.05$) in WT mice following 48 h food deprivation (Figure 6G,H). Total FOXO1 levels in myonuclei were also significantly increased by 2-fold after 24 h in mKO animals versus their fed mKO littermates. Compared to the WT fed group, total FOXO3 levels in myonuclei were significantly greater by 3-fold in WT animals following 48 h of food deprivation, whereas nuclear FOXO3 content was similar between fed and fasted conditions in mKO mice. Nuclear FOXO3 phosphorylation status was lower by ~65% ($p < 0.05$) in fed and fasted mKO mice versus the fed WT condition. Furthermore, relative to WT fed animals, fasting induced a significant ~50% reduction in FOXO3 phosphorylation status in WT myonuclei after 24 and 48 h. Nuclear FOXO3 phosphorylation status was similar between fed and fasted conditions in mKO mice.

A significant interaction between genotype and fasting for nuclear TFEB protein content emerged (Figure 6G,I). To complement these data, fed and fasted EDL muscle cross-sections from WT and mKO animals were stained for wheat germ agglutinin (WGA), 4',6-diamidino-2-phenylindole dihydrochloride (DAPI), and TFEB to assess TFEB myonuclear localization (Figure 6J). Compared to the WT fed group, the amount of TFEB-positive myonuclei was significantly elevated by 1.8-fold in WT muscle after 24 and 48 h of food deprivation (Figure 6K). Contrary to this, TFEB-positive myonuclei in mKO mice was similar between fed and fasted conditions.

Effects of fasting on CARM1 activity and autophagy signaling in human skeletal muscle

Prolonged food deprivation in humans elicits protein breakdown [35,36], but its impact on CARM1 activity in human skeletal muscle remains to be elucidated. To investigate this, skeletal muscle biopsies were collected from the vastus lateralis QUAD muscles of healthy, young men 1 h postprandial and again after 48 h of food deprivation. We observed a decrease in myofiber CSA in six of nine participants, and mean myofiber CSA exhibited a 10% reduction ($p = 0.12$) in

(normal and long exposures) in mitochondria isolated from QUAD muscles of WT and mKO animals following fasting. Blots are accompanied by a typical Ponceau stain and molecular masses (kDa) are shown at the right of blots. (G) graphical summary of western blot data comprising mitochondrial PRKN protein content in WT and mKO mice during fed and 48 h fast conditions. Data are expressed as protein content relative to WT fed ($n = 10-13$). (H) Representative images of EDL muscle cross sections stained for PRKN (red; scale bar: 2 μm) and TOMM20 (green; scale bar: 1 μm) with a merged image. (I) graphical summary of PRKN puncta in WT and mKO mice following food deprivation assessed by immunofluorescence. Data are expressed as number of PRKN puncta per 1,000 μm^2 ($n = 3$). (J) *Prkn*, *Bnip3* (BCL2 interacting protein 3) mRNA expression in EDL muscles from WT and mKO mice under fed and fast conditions. Data are expressed as mRNA content relative to WT fed ($n = 11-13$). (K) Representative western blots of PRKN and BNIP3 in WT and mKO TA muscles after fasting, accompanied by a typical Ponceau stain. Molecular masses (kDa) are shown at the right of blots. (L) graphical summary of PRKN and BNIP3 protein expression levels in WT and mKO animals during fed and fast conditions. Data are expressed as protein content relative to WT fed ($n = 11-18$). Data are means \pm SEM. Two-way ANOVA; § $p < 0.05$ interaction effect of genotype and fasting; ¶ $p < 0.05$ main effect of genotype; † $p < 0.05$ main effect of fasting; § $p < 0.05$ main effect of Col; ¶ $p < 0.05$ versus WT fed; # $p < 0.05$ versus mKO Fed.

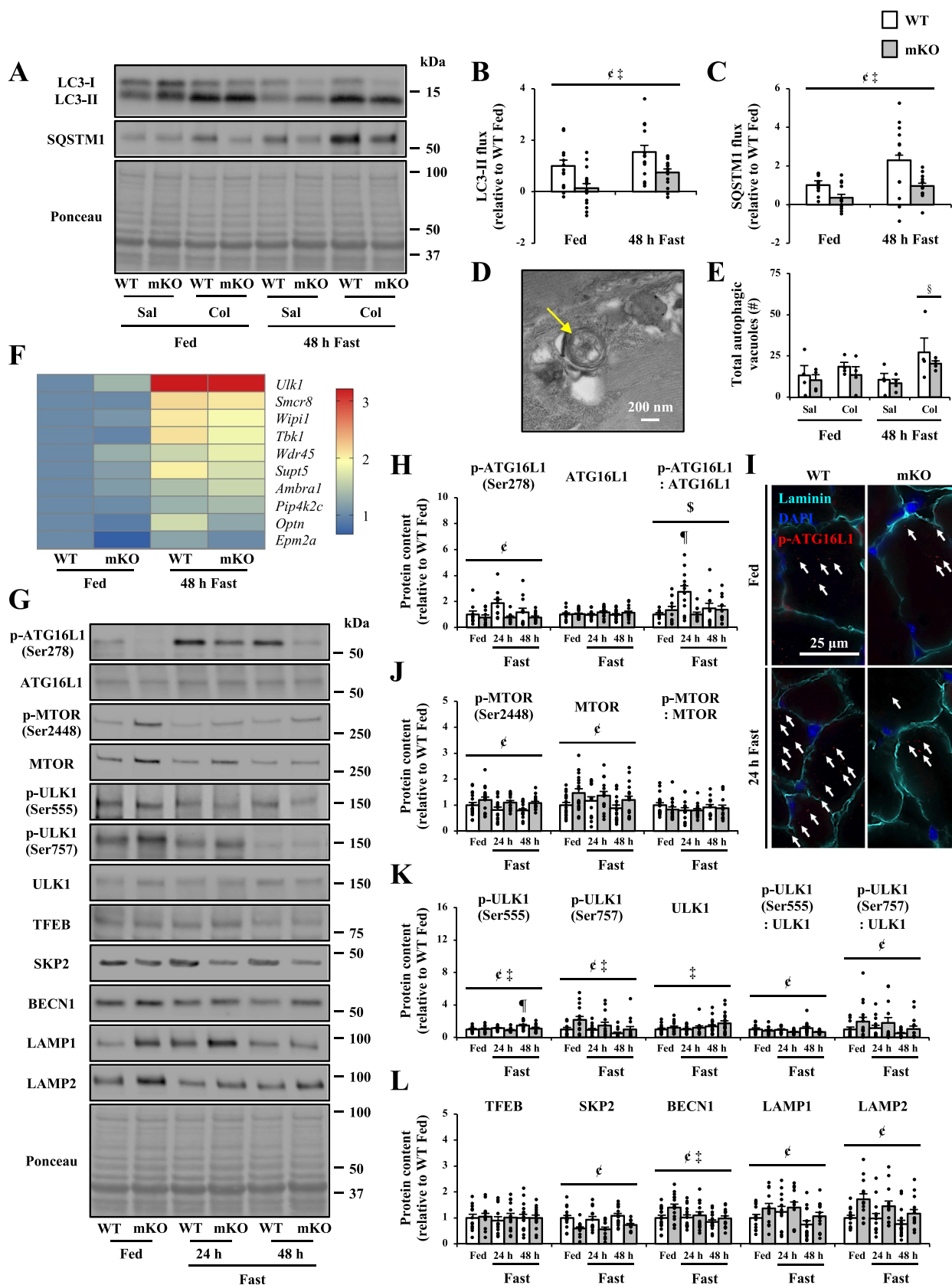


Figure 5. Skeletal muscle autophagy is dysregulated in mKO animals during atrophy. (A) Representative western blots of LC3-I, LC3-II, and SQSTM1 in TA muscles of WT and mKO mice treated with Sal or Col under fed and 48 h fast conditions, accompanied by a typical Ponceau stain. Molecular masses (kDa) are shown at the right of blots. (B-C) Graphical summaries of LC3-II and SQSTM1 flux in WT and mKO animals under fed and 48 h fast conditions. Data are expressed as protein content relative to WT fed ($n = 12-16$). (D) Representative image from mKO muscle of double-membrane autophagic vacuole (yellow arrow). Scale bar: 200 nm. (E) Graphical summary of total number of autophagic vacuoles in WT and mKO mice treated with Sal or Col under fed and 48 h fast conditions. (F) Heatmap of macroautophagy genes in TA muscle with enrichment unique to *carml* mKO after fasting. Data are expressed relative to WT fed ($n = 3$). (G) Typical western blots of phosphorylated autophagy-related 16 (p-ATG16L1 [Ser278]), total ATG16L1, phosphorylated (p)-MTOR (mechanistic target of rapamycin kinase; Ser2448), total MTOR, p-ULK1 (unc-51 like autophagy activating kinase 1; Ser555), p-ULK1 (Ser757), total ULK1, TFEB (transcription factor EB), SKP2 (S-phase kinase associated protein 2), BECN1, LAMP1

healthy males following 48 h of fasting (Figure 7A,B), while myofiber CSA distribution also skewed smaller ($p = 0.16$) after food deprivation (Figure 7A,C). Previous work demonstrated the effect of a 40 h fast on global mRNA expression in human QUAD muscle [37]. These authors found that the transcript levels of *Carm1* and its *Prmt* family members were similar in fed versus fast conditions (Figure 7D). At the protein level, CARM1 content was unchanged in human QUAD muscle after 48 h of fasting (Figure 7E,F). We next assessed asymmetric arginine dimethylation of pan-CARM1-marked substrates [28,29], along with SMARCC1 me2a (Arg1064), and PABPC1 me2a (Arg455/Arg460). We detected a strong trend ($p = 0.07$) for lower CARM1 substrate methylarginine content in human skeletal muscle following 48 h of food deprivation compared to the fed condition (Figure 7E,G). Relative to fed muscle, there was also a 25% decrease in methylated SMARCC1 me2a (Arg1064; $p = 0.15$) and total SMARCC1 ($p = 0.17$) protein content after 48 h of fasting (Figure 7E,H). Furthermore, food deprivation in healthy humans led to a significant 55% decrease in methylated PABPC1 me2a (Arg455/Arg460) and reduced ($p = 0.12$) total PABPC1 protein content versus the fed condition (Figure 7E,I).

We next sought to examine whether the many tendencies in the data strongly suggesting fasting-induced myofiber atrophy and CARM1 activity were accompanied by the induction of early molecular markers of autophagy signaling. Others have demonstrated that genes related to the autophagy-lysosome and ubiquitin-proteasome proteolytic systems were upregulated in healthy human adults after 40 h of food deprivation [37]. In the current study, levels of mitophagy proteins PRKN ($p = 0.20$) and BNIP3 ($p = 0.14$) trended upward in healthy male humans after 48 h of fasting (Figure 7E,I,K). We found that compared to muscle from participants in the fed condition, 48 h of fasting induced a significant ~2-fold increase in LC3-II protein (Figure 7E,L). There was also a strong trend ($p = 0.07$) toward greater p-ATG16L1 (Ser278) protein content in human skeletal muscle after 48 h of fasting relative to the fed condition (Figure 7E,M). We detected a significant ~40% decrease in p-ULK1 (Ser757) and a 1.4-fold increase ($p < 0.05$) in total ULK1 protein content in fasted muscle compared to fed conditions (Figure 7E,N). The ULK1 phosphorylation status was significantly lower by 60% in fasted versus fed human muscle.

Discussion

In this study, we confirm that CARM1 is required to maintain muscle mass and show that muscle-specific deletion of *Carm1* attenuates the progression of fasting-induced muscle wasting. We provide evidence that *carm1* mKO remodels skeletal muscle toward a slower, more oxidative myogenic program. This was supported by increased gene expression of downstream PPARGC1A targets *Tfam* and *Nfe2l2*, plus greater PPARGC1A

splicing activity in mKO versus WT animals. Skeletal muscle-specific removal of *Carm1* also resulted in perturbed mitophagic, autophagic, and atrophic signaling downstream of AMPK, MTOR, and AKT under fed and fasted settings. Specifically, we provide evidence that knockout of *Carm1* in muscle led to dysregulated AMPK site-specific activation of ULK1 (Ser555), FOXO3 (Ser413), and FOXO3 (Ser588), as well as MTOR targeted inhibition of ULK1 (Ser757), along with AKT site-specific suppression of FOXO1 (Ser256) and FOXO3 (Ser253). Moreover, fasting altered CARM1 biology within the context of early markers of autophagy signaling at threshold of atrophy in human skeletal muscle. Collectively, this study supports and extends earlier work characterizing CARM1 expression and function in human skeletal muscle in vivo, as well as demonstrates that CARM1 is a powerful regulator of autophagy [24,33,34,38,39], particularly in skeletal muscle [6,15,21,22], along with mitophagic and atrophic processes critical for the maintenance and remodeling of muscle mass.

The present study provides further evidence that CARM1 is required to maintain muscle mass under fed conditions. Consistent with our recent work [6,15], we demonstrate that muscle-specific knockout of *Carm1* leads to aberrant autophagic processes and elevated muscle atrophy. This aligns with the unique muscle atrophy gene signature observed in mKO versus WT mice during fed settings [6], and the abundance of evidence suggesting that autophagy is required to maintain muscle mass [40]. We now present evidence that *carm1* mKO mitigates both fasting- and denervation-induced skeletal muscle wasting [15,21] despite the complementary, but in some respects disparate molecular signatures of these atrophy-inducing stimuli [41,42]. It remains unclear whether this is due to a protective effect of *carm1* deletion, or possibly to mKO muscles already reaching maximal atrophy, or a combination of both. Future experiments should employ an inducible *carm1* mKO model [43], and/or pharmacological inhibition of CARM1 [16,44], to control for any compensatory or confounding adaptations that may have occurred perinatally or during maturation in mKO animals. The impact of overexpressing and/or pharmacologically activating CARM1 in skeletal muscle should also be investigated under basal and atrophying conditions to elucidate this further. Notably, although muscles atrophied to a similar extent during conditions of neurogenic muscle disuse and fasting, we observed in PRMT content and methyltransferase activity, including CARM1, a general upregulation with denervation [15] but largely no effects in response to fasting except for specific reductions in CARM1 function revealed by decreased SMARCC1 me2a (Arg1064) and PABPC1 me2a (Arg455/Arg460) levels. These findings indicate that the impact of CARM1, as well as that of other PRMTs, on atrophy-evoked remodeling is at least in part dependent on the mode of skeletal muscle wasting.

It was previously shown that AMPK-dependent stabilization of CARM1 upregulates autophagy [24], and that CARM1

(lysosomal associated membrane protein 1), and LAMP2 in WT and mKO TA muscles after food deprivation, accompanied by a Ponceau stain. Molecular masses (kDa) are shown at the right of blots. (H) Graphical summaries of p-ATG16L1 (Ser278), ATG16L1, ATG16L1 phosphorylation status. (I) Representative images of EDL muscle cross sections stained for laminin (aqua), DAPI (4',6-diamidino-2-phenylindole dihydrochloride; blue), and p-ATG16L1 (Ser278; red). White arrows indicate p-ATG16L1 (Ser278) puncta. Scale bar of merged image: 25 μ m ($n = 3$). (J-L) Graphical summaries of p-MTOR (Ser2448), MTOR, MTOR phosphorylation status, p-ULK1 (Ser555), p-ULK1 (Ser757), ULK1, ULK1 phosphorylation statuses, TFEB, SKP2, BECN1, LAMP1, and LAMP2 protein expression in WT and mKO animals following fasting. Data are expressed as protein content relative to WT fed ($n = 9-18$). Data are means \pm SEM. Two-way ANOVA; § $p < 0.05$ interaction effect of genotype and fasting; ¶ $p < 0.05$ main effect of genotype; † $p < 0.05$ main effect of fasting; ‡ $p < 0.05$ main effect of Col; ¶ $p < 0.05$ versus WT fed.

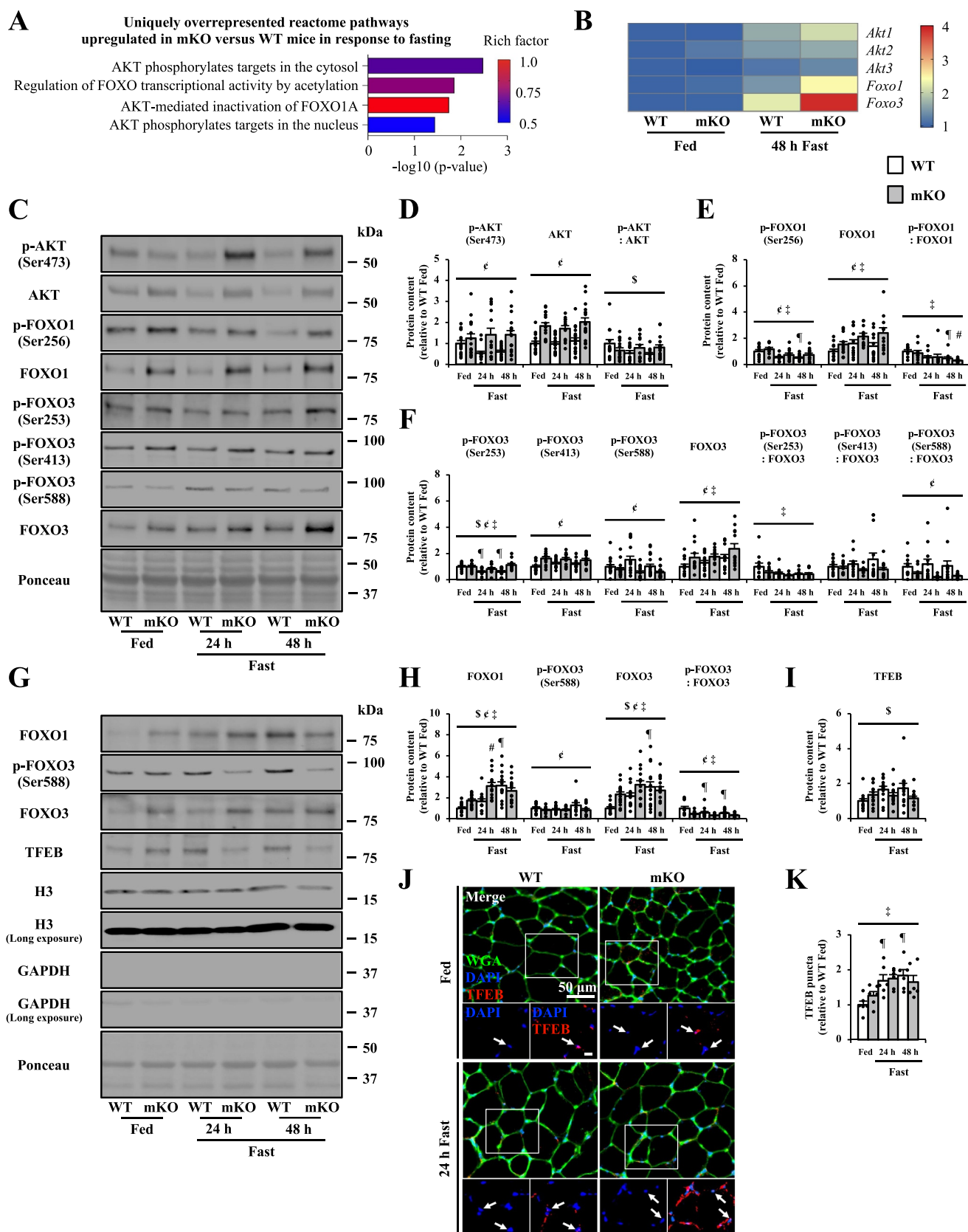


Figure 6. Altered atrophic signaling and myonuclear localization of catabolic proteins in mKO animals after fasting. (A) uniquely overrepresented upregulated reactome pathways in mKO versus WT mice following 48 h fast ($n = 3$). (B) heatmap of *Akt1*, *Akt2*, *Akt3*, *Foxo1*, and *Foxo3* genes in TA muscle of WT and mKO mice after fasting. Data are expressed relative to WT fed ($n = 3$). (C) Representative western blots of p-AKT (Ser473), total AKT, p-FOXO1 (forkhead box O1; Ser256), total FOXO1, p-FOXO3 (Ser253), p-FOXO3 (Ser413), p-FOXO3 (Ser588), and total FOXO3 in WT and mKO TA muscles after food deprivation, accompanied by a typical Ponceau stain. Molecular masses (kDa) are shown at the right of blots. (D-F) graphical summaries of p-AKT (Ser473), AKT, AKT phosphorylation status, p-FOXO1 (Ser256), FOXO1, FOXO1 phosphorylation status, p-FOXO3 (Ser253), p-FOXO3 (Ser413), p-FOXO3 (Ser588), FOXO3, and FOXO3 phosphorylation statuses in WT and mKO animals in response to fasting. Data are expressed as protein content relative to WT fed ($n = 10-18$). (G) Representative western blots of total FOXO1, p-FOXO3 (Ser588), total FOXO3, TFEB, histone H3 (normal and long exposures), and GAPDH (normal and long exposures) in myonuclei isolated from WT and mKO GAST

reciprocally modulates AMPK and its downstream signaling network in skeletal muscle [15]. Importantly, AMPK activation promotes muscle wasting and the loss of AMPK in muscle protects against the removal of mitochondria tagged for autophagic degradation [45,46]. We found that AMPK phosphorylation status was significantly greater in WT mice after food deprivation, whereas no changes were observed between fed and fasted conditions in mKO animals. The attenuation of fasting-induced atrophy in faster, more glycolytic muscles of mKO mice was likely due, at least in part, to lower AMPK activation, along with higher expression and activity of the transcriptional coactivator PPARGC1A in mKO mice. A high level of PPARGC1A enhances mitochondrial function and preserves mitochondrial mass by minimizing targeting of the organelle for degradation in response to denervation- and fasting-induced atrophy [47]. Consistent with this, *carm1* mKO led to increased gene expression of downstream PPARGC1A targets *Tfam* and *Nfe2l2*, along with greater PPARGC1A splicing activity. Accordingly, mitochondrial content was maintained in mKO mice in response to food deprivation and *carm1* mKO resulted in a shift toward slower MYH isoform expression, increased SDH activity, and greater oxidative capacity in fast-twitch muscle. Thus, we postulate that *carm1* mKO mitigates the progression of fasting-induced atrophy by evoking a shift toward a slower, more oxidative myogenic program, which is more resistant to atrophy-inducing stimuli during fasting, disuse, and disease conditions [48].

Knocking out *Carm1* in skeletal muscle inhibited mitophagy and autophagy flux under basal conditions. Although mitophagy and autophagy flux increased in mKO mice in response to food deprivation, levels of mitophagy protein PRKN in mitochondria did not change in mKO animals during fasting. PRKN puncta, which tag mitochondria for degradation, were elevated in WT animals as early as 24 h after food deprivation, whereas similar accumulations of PRKN were detected between fed and fasted conditions in mKO mice. *carm1* mKO also resulted in aberrant buildup of total PRKN and BNIP3 protein content in whole muscle after fasting. Despite these disparate mitophagic adaptations in mKO mice in response to food deprivation, it remains unclear whether the observed changes in response to fasting are a direct impact of *carm1* loss, or secondary to changes occurring in the animals across a lifetime without the enzyme. It is tempting to attribute the distinct mitophagic adaptations to altered processes downstream of AMPK and overexpression of PPARGC1A in mKO muscle determined in this work. When considering this possibility, it should be noted that AMPK deletion delays PRKN activation [49]. Mitochondrial fragmentation is also required for proper

mitochondrial turnover to occur, and PPARGC1A strongly promotes organelle fusion [50]. Future examinations of mitophagy and mitochondrial dynamics will assist in uncovering the role of CARM1-AMPK-PPARGC1A signaling in the regulation of skeletal muscle mass.

A main finding of the current study is that loss of *carm1* alters the autophagy-lysosome system in skeletal muscle during fasting-evoked muscle atrophy. Following food deprivation, *carm1* mKO resulted in reduced phosphorylation of ATG16L1 (Ser278), which serves as a surrogate for ULK1 activity and directly corresponds to autophagy induction [51]. Consistent with this, we observed lower levels of AMPK-mediated ULK1 (Ser555) phosphorylation, a canonical marker of autophagic activation [31,40], in mKO versus WT muscle after fasting. Our data suggest that muscle-specific deletion of *Carm1* may hinder autophagy flux in response to food deprivation, evidenced by lower ATG16L1 (Ser278) phosphorylation levels during 24 h-fasted conditions. In addition to the macroautophagy genes with enrichment unique to *carm1* mKO after fasting, the upregulation of BECN1, LAMP1, and LAMP2 in mKO versus WT muscle during food deprivation further implies that muscle-specific deletion of *Carm1* leads to dysregulated autophagosome processing and defective lysosomal clearance. These results support the assertion that *carm1* mKO modulates fasting-induced muscle atrophy through autophagy inhibition.

Since hyperactivation of MTOR (Ser2448) is sufficient to block autophagy and mitigate muscle wasting in response to fasting [35,52], in part through marking of ULK1 (Ser757) [31], it is reasonable to speculate that sustained phosphorylation of MTOR (Ser2448) and ULK1 (Ser757) in mKO muscle at baseline and during food deprivation played a key role in attenuating protein breakdown. Moreover, CARM1 interacts with TFEB in myonuclei, and the absence of the methyltransferase influences nuclear TFEB protein levels during fasting-induced muscle atrophy. Since MTOR fosters TFEB nuclear export [53], we reason that hyperphosphorylation of MTOR (Ser2448) in mKO mice contributes to impeded TFEB nuclear entry during food deprivation. Despite the relatively lower TFEB myonuclear localization in mKO animals, mRNA levels of TFEB-dependent autophagy and lysosomal genes were similarly induced in WT and mKO mice with fasting, which suggests enhanced TFEB transcriptional activity and/or compensatory mechanisms involving TFEB family members, such as TFE3 [54–56]. Interestingly, myonuclear TFEB content was elevated in WT animals 24 h following food deprivation, which likely facilitated AMPK-dependent TFEB transcriptional activity [57]. Furthermore, our transcriptomic analyses uncovered muscle hypertrophy (GO:0014743) as a biological process that was regulated by *carm1* mKO in response to food deprivation. We reason that augmented phosphorylation of AKT (Ser473) and downstream MTOR (Ser2448) in mKO muscle resulted from heigh-

muscles following food deprivation, accompanied by a typical Ponceau stain. Molecular masses (kDa) are shown at the right of blots. (H-I) graphical summaries of myonuclear FOXO1, p-FOXO3 (Ser588), FOXO3, FOXO3 phosphorylation status, and TFEB protein content in WT and mKO mice after fasting. Data are expressed as nuclear protein content relative to WT fed ($n = 12-15$). (J) Representative images of EDL muscle cross sections stained for wheat germ agglutinin (WGA; green), DAPI (blue), and TFEB (red). Scale bar of merged image: 50 μm . Higher magnifications are inset with TFEB-positive myonuclei (white arrows). Scale bar of inset: 10 μm . (K) graphical summary of nuclear TFEB content in WT and mKO animals following food deprivation. Data are expressed as TFEB-positive myonuclei relative to WT fed ($n = 6$). Data are means \pm SEM. Two-way ANOVA; § $p < 0.05$ interaction effect of genotype and fasting; c $p < 0.05$ main effect of genotype; ‡ $p < 0.05$ main effect of fasting; ¶ $p < 0.05$ versus WT fed; # $p < 0.05$ versus mKO Fed.

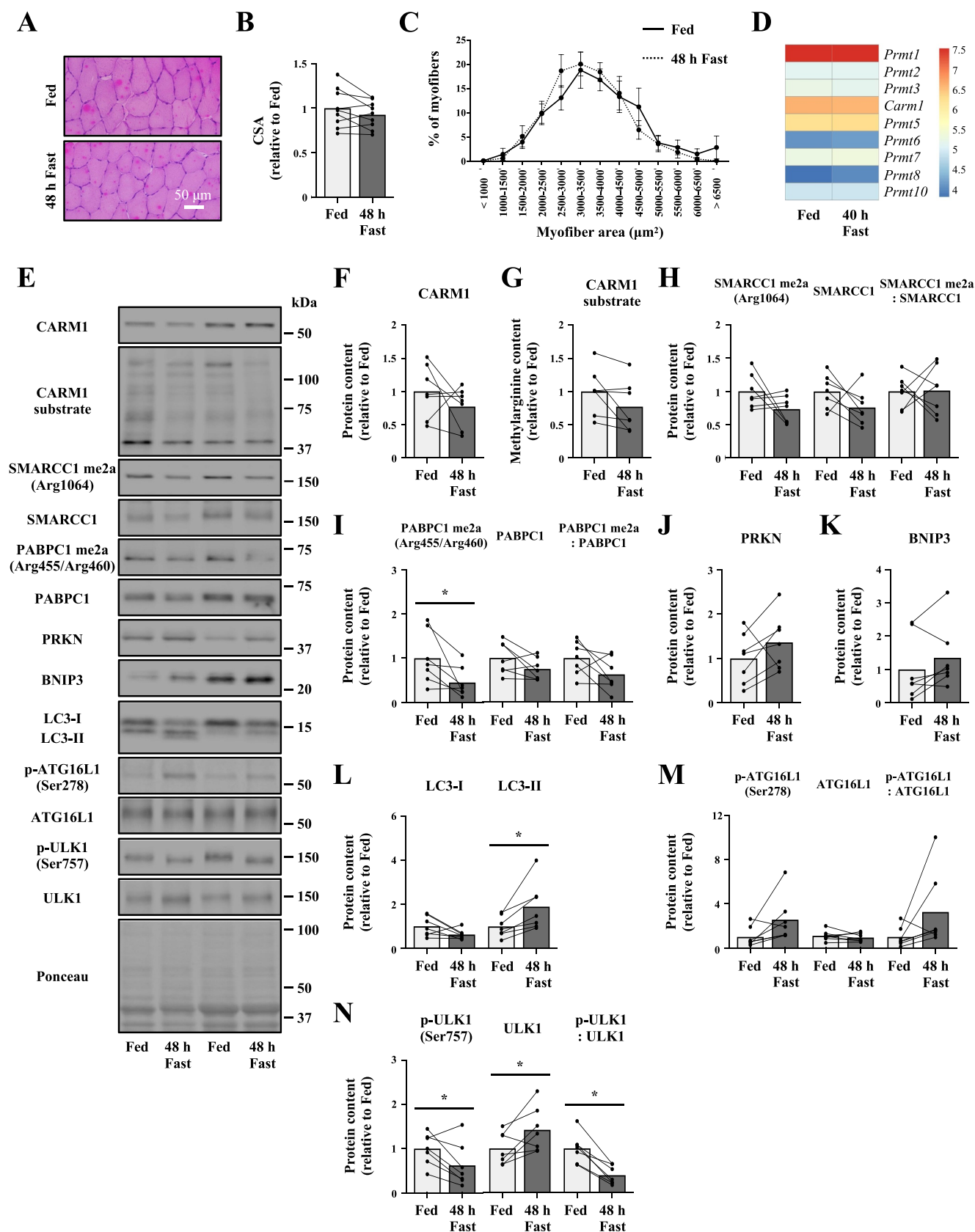


Figure 7. The impact of fasting on human skeletal muscle fiber size, CARM1 biology, and atrophy- and autophagy-related signaling. (A) Representative images of H&E-stained vastus lateralis QUAD muscle cross sections of healthy male participants collected 1 h postprandial (fed) and following 48 h of fasting (fast). Scale bar: 50 μ m. (B) graphical summary of the average myofiber CSA of QUAD muscles from adult humans in response to fasting. Data are expressed as CSA relative to fed ($n = 9$). (C) distribution of CSA (μ m²) in QUAD of fed (solid line) and fast (dashed line) human myofibers ($n = 9$). (D) heatmap visualizing the average mRNA expression of PRMT family members in QUAD muscle of adult humans during fed and 40 h fast conditions. Microarray data extracted from GSE28016 ($n = 7$). (E) Representative western blots of CARM1, asymmetric arginine dimethylated CARM1 substrates, SMARCC1 me2a (Arg1064), total SMARCC1, PABPC1 me2a (Arg455/Arg460), total PABPC1, PRKN, BNIP3, LC3-I, LC3-II, p-ATG16L1 (Ser278), total ATG16L1, p-ULK1 (Ser757), and total ULK1 in QUAD muscles from healthy humans in response to 48 h of fasting, accompanied by a typical Ponceau stain. Molecular masses (kDa) are shown at the right of blots. (F-N) graphical summaries of CARM1, CARM1 substrate,

tened sensitivity to insulin/insulin-like growth factor 1 signaling and led to preserved MPS (muscle protein synthesis) [58] during fasting. Altogether, these data suggest that *carm1* mKO curtails fasting-induced muscle wasting via alterations in autophagy-lysosomal machinery and MPS signaling pathways in addition to the transcriptional and post-translational events established here. Further work is necessary to confirm this possibility and to identify the key players.

AKT and AMPK modulate muscle protein breakdown via the downstream FOXO transcriptional network [58]. For instance, AKT-induced phosphorylation of FOXO1 (Ser256) and FOXO3 (Ser253) suppresses FOXO-dependent atrogene expression by promoting its nuclear exclusion [59,60]. Our transcriptomic data suggest that pathways involved in AKT signaling, including the regulation of FOXO transcriptional activity, are upregulated in mKO mice after fasting. We show that phosphorylation of FOXO1 (Ser256) and FOXO3 (Ser253) decreased in WT mice following food deprivation, whereas no changes were detected in mKO animals between fed and fasted conditions. Concomitantly, knocking out *Carm1* in skeletal muscle blunted the accumulation of myonuclear FOXO1 and FOXO3 protein content after food deprivation. Since deletion of FOXOs spares muscle loss during food deprivation, in part, by preventing the induction of atrogens [41], and CARM1 is required for FOXO3 transcriptional activity during neurogenic muscle disuse [21], it is reasonable to posit that *carm1* mKO, in part, protects against fasting-induced atrophy by inhibiting FOXO-dependent protein degradation. Unlike AKT, AMPK promotes the transcription of atrogens by phosphorylating FOXO3 (Ser588) and FOXO3 (Ser413) [32]. Notably, AMPK phosphorylation at both FOXO3 residues upregulates the transcription of *Trim63* and *Fbxo32*, independent of FOXO3 subcellular localization. Consistent with our data and previous work [15], knocking out *Carm1* in muscle led to decreased phosphorylation of FOXO3 (Ser588) in the myonuclear compartment. Interestingly, phosphorylation of FOXO3 (Ser413) was greater in mKO versus WT muscle, possibly to compensate for reduced phosphorylation at the FOXO3 (Ser588) site, as interplay between AMPK-specific FOXO3 residues has been previously observed [61]. This aligns with food deprivation evoking a similar increase in *Trim63* and *Fbxo32* atrogene mRNA content between genotypes. Future studies should focus on investigating the impact of CARM1 on FOXO-specific atrogens during atrophy, in order to further our understanding of the role of the methyltransferase in muscle protein breakdown.

Our results show that fasting influences CARM1 activity similarly in human and murine skeletal muscle amid the inception and early progression of atrophy and autophagy. Although our human results were limited by statistical power, as well as by the interrogation of a single sex, muscle, and timepoint, we show that methylation of validated CARM1 targets was reduced following fasting. For instance,

asymmetric arginine dimethylation of PABPC1 me2a (Arg455/Arg460) significantly decreased in both murine and human skeletal muscle after 48 h of food deprivation. Thus, data from our animal and human studies highlight the translational relevance of the current findings. Further preclinical research is needed to advance our mechanistic understanding of CARM1 and to determine whether manipulating its expression and/or activity is a viable approach for preserving muscle mass in clinical settings that evoke atrophy.

In summary, *carm1* mKO mice displayed reduced muscle mass, as well as aberrant mitophagic, autophagic, and atrophic signaling downstream of AMPK, MTOR, and AKT in skeletal muscle. The absence of *Carm1* also elicited PPARGC1A activity and a slower, more oxidative muscle phenotype, which altogether served to attenuate fasting-induced muscle wasting. Together with recent observations that demonstrate an attenuation of neurogenic muscle atrophy in *carm1* mKO [15] and knockdown [21] conditions along with reports of CARM1-mediated control of autophagy [24,39], these data indicate that CARM1 is a nexus effector molecule remarkably responsive to atrophy- and autophagy-inducing stimuli. Indeed, CARM1 activity decreased similarly in murine and human skeletal muscle after food deprivation, also underscoring the translational impact of the methyltransferase in human muscle biology. Further investigation is warranted to determine whether CARM1 is a viable therapeutic target for combating muscle wasting in alternative pre-clinical and clinical settings characterized by dysregulated mitophagic, autophagic, and atrophic signaling, such as the sarcopenia of aging, cancer cachexia, and neuromuscular disorders.

Materials and methods

Animal model and fasting experiments

WT and mKO mice were housed in the McMaster Animal Facilities and all protocols were approved by the Animal Research Ethics Board at McMaster University operating under the regulations of the Canadian Council for Animal Care. CARM1 floxed animals with C57BL6J/129 background [7,62] were a kind gift from Dr. Mark Bedford (The University of Texas MD Anderson Cancer Centre, Smithville, TX, USA). CARM1 homozygous floxed (WT) mice served as a control in this study. We employed the Cre/loxP system to generate mKO mice as described previously [15]. Briefly, CARM1 floxed animals were crossed with human ACTA1/ α -skeletal actin-Cre mice (Jackson Laboratories Strain 006,149) expressing skeletal muscle-specific Cre recombinase [43]. Progeny were genotyped by obtaining tail clippings for DNA extraction, as well as by performing reverse transcription-polymerase chain reaction (RT-PCR) and gel electrophoresis protocols. The following primers were used to verify that WT and mKO mice contained a LoxP site for *Carm1* between exon 2 and 3: forward (F)-AGTTGGTGACCCTTGTGTCC, reverse (R)-AGCTGC CAGGACCTCTGATA. The following primers were used to

detect mKO mice that express Cre recombinase: F-GCGGTCTGGCAGTAAAACTATC, R-GTGAAACAGCAT TGCTGCTCACTT. WT and mKO animals were studied at 12-weeks of age (~25 g body mass; male) and were housed in an environmentally controlled room (23°C, 12-h light/12-h dark cycle). During fasting experiments, food was removed from mice at the beginning of the active light cycle for a total of 24 or 48 h prior to sacrifice and tissue collection. Fed, control mice maintained ad libitum access to food and were sacrificed at the same time as their fasted littermates. Animals ($n = 11$ –21/group) were euthanized via cervical dislocation. TA, QUAD, GAST, EDL, and SOL muscles were rapidly excised, weighed, frozen in liquid nitrogen or mounted in optimal cutting temperature compound (OCT; Thermo Fisher Scientific Life Sciences, 23-730-571) then frozen in isopentane cooled with liquid nitrogen. All muscles were then stored at -80°C for subsequent biochemical analyses.

Fasting studies in healthy human participants

Participants (age = ~22 years; $n = 10$; male) underwent food deprivation. Muscle biopsies were collected from the vastus lateralis quadriceps 1 h postprandial and following 48 h of fasting. The study was approved by the Health Sciences Research Ethics Board at Queen's University and conformed to the Declaration of Helsinki. Materials and methods from this data set, including participant characteristics and experimental design, have been published previously [63,64].

Autophagy and mitophagy flux calculation. To determine the relative degree of autophagosome and mitochondrial turnover, WT and mKO mice received intraperitoneal injections of colchicine (Col; 0.4 mg/kg/day; Thermo Fisher Scientific Life Sciences, AC227125000) or an equal volume of 0.9% saline (Sal) every 24 h for two days prior to the day of sacrifice ($n = 12$ –16/group). This dosage of Col is sufficient to disrupt microtubules and inhibit autophagosome-lysosome fusion for autophagic and mitophagy flux calculations [65,66]. Animals were randomly assigned to either fed or 48 h fasted groups. Western blotting (as described below) of LC3-II and SQSTM1 was performed in TA whole muscle or QUAD mitochondrial fraction samples with all conditions represented on one SDS-PAGE gel. LC3-II and SQSTM1 protein content was quantified using ImageJ and values were corrected for loading via Ponceau S solution (Sigma-Aldrich, P7170). Autophagic flux was calculated based on the difference in LC3-II or SQSTM1 levels between Col- and Sal-treated mice (i.e., fed WT Col – mean fed WT Sal) as described previously [31,66].

RNA sequencing and analysis. Global transcriptional changes in mKO versus WT animals in response to fasting was examined using RNA-seq analysis in TA muscles as described previously [6]. All work was performed based on Illumina Stranded mRNA Prep Reference Guide (April 2021) and accepted Standard Operating Procedures (SOPs) in place within StemCore Laboratories.

Total RNA was initially purified from powdered frozen muscle tissue in TRIzol (Thermo Fisher Scientific Life Sciences 15,596,018) using a standard chloroform extraction protocol. Quantity and quality of total RNA was then measured and assessed for library construction. Total RNA

concentration was measured using 1 μl of sample with the Qubit HS RNA assay (Thermo, Q32852) and RNA quality was assessed on the Fragment Analyzer Standard Sensitivity RNA assay (Agilent). An RNA Quality Number (RQN) above 8.0 was required for library processing. DNA libraries were then prepared using the Illumina Stranded mRNA Prep Kit (Illumina 20,040,532) using 25–1000 ng of total RNA. Quantification of the libraries were performed using the Qubit Double Stranded DNA HS kit (Thermo, Q33230). The AATI Fragment Analyzer with the High Sensitivity NGS assay (Agilent) was used to verify the size distribution of the template library.

The DNA libraries were normalized, pooled, and diluted as required to achieve acceptable cluster density on the Illumina NextSeq 500 sequencer. The library pool then underwent 1×75 cycles of single-end sequencing with the Illumina NS500 75 cycle high output kit, providing up to 60 million reads per sample.

Whole muscle protein extraction. Tissues were processed as described previously [10,15]. For total protein extraction, frozen QUAD or TA muscles were pulverized to a fine powder with a mortar and pestle on liquid nitrogen. Muscle samples were suspended in RIPA buffer (Sigma-Aldrich, R0278), supplemented with cComplete Mini Protease Inhibitor Cocktail (Sigma-Aldrich 05,892,970,001) and PhosSTOP Phosphatase Inhibitor Cocktail (Sigma-Aldrich, PHOSS-RO). Further homogenization was performed using stainless steel lysing beads and TissueLyser (Qiagen, Hilden, NRW, Germany) at a frequency of 30 Hz for 5 min. Lysates were then mixed by end-over end inversion for 60 min at 4°C followed by centrifugation at $14,000 \times g$ for 10 min. The supernatants were collected, and protein concentrations were determined using the BCA protein assay (Thermo Fisher Scientific Life Sciences, PI23225). Samples were then stored at -80°C for further analysis.

Mitochondria, nuclear and cytosolic isolations. Mitochondria, nuclear and cytosolic fractions were isolated from QUAD and GAST muscles as described previously [10,67]. Briefly, frozen tissue was suspended in STM buffer (250 mM sucrose, 50 mM Tris – HCl, pH 7.4, 5 mM MgCl_2 , protease and phosphatase inhibitors) and minced with sharp scissors on ice. Samples were then homogenized with a micropestle for 2 min. After incubating on ice for 30 min, samples were vortexed, followed by centrifugation at $800 \times g$ for 15 min. The pellet and supernatant were separated for isolating nuclear and cytosolic fractions, respectively. To isolate the nuclear fraction, the pellet was resuspended in STM buffer, vortexed, and then centrifuged at $500 \times g$ for 15 min. After repeating the previous centrifugation step at $1,000 \times g$ for 15 min, pellet was suspended in NET buffer (20 mM HEPES, pH 7.9, 1.5 mM MgCl_2 , 0.5 M NaCl, 0.2 mM EDTA, 20% glycerol, 1% Triton X-100 [Sigma-Aldrich, X100], protease and phosphatase inhibitors), which was then vortexed and placed on ice for 30 min. Next, samples were sonicated and centrifuged at $9,000 \times g$ for 30 min to yield the nuclear fraction. To isolate the cytosolic fraction, the supernatant set aside earlier also underwent a series of centrifugation steps. Mitochondria from these steps were further isolated by resuspending the

pellet in mitochondrial isolation buffer (50 mM Tris HCl, pH 6.8, 1 mM EDTA, 0.5% Triton X-100, protease and phosphatase inhibitors). Protein concentrations were determined using the BCA protein assay (Thermo Fisher Scientific Life Sciences, PI23225) and fractions were stored at -80°C for further analysis.

Western blotting. Proteins extracted from whole muscle, as well as mitochondria, nuclear and cytosolic compartments, were separated on 10% SDS-PAGE gels or 4–15% precast gradient gels (Bio-Rad Laboratories, Inc., 5678085) and subsequently transferred onto nitrocellulose membranes. Following transfer, membranes were stained with Ponceau S solution (Sigma-Aldrich, P7170) to serve as a loading control [10,15,68]. Membranes were then washed with $1 \times$ TBST (20 mM Tris, 150 mM NaCl, 0.1% Tween 20 [Thermo Fisher Scientific Life Sciences, BP337500] detergent) and blocked with 5% BSA (BioShop, ALB007)-TBST for 1 h before being incubated in a primary antibody overnight at 4°C with gentle rocking. The next day, blots were washed with $1 \times$ TBST and incubated in the appropriate secondary antibody (1:2,000; Cell Signaling Technology, 7074S) conjugated to horseradish peroxidase with gentle rocking at room temperature for 1 h. Blots were then washed again with $1 \times$ TBST, followed by visualization with enhanced chemiluminescence (Bio-Rad Laboratories, Inc., 1705060). Blots were developed with long and short exposures. Protein density was analyzed by a blinded investigator using ImageJ.

We employed antibodies against CARM1 (1:5,000; Bethyl Laboratories, A300-421A), PRMT1 (1:1,000; EMD Millipore, 07-404), PRMT5 (1:1,000; EMD Millipore, 07-405), PRMT6 (1:1,000; Bethyl Laboratories, A300-929A), PRMT7 (1:1,000; Santa Cruz Biotechnology, sc -376,077), MMA (1:1,000; Cell Signaling Technology, 8015S), ADMA (1:1,000; 13522S; Cell Signaling Technology, 13522S), CARM1 substrate (1:1,000; another gift from Dr. Mark Bedford, MD Anderson Cancer Center, University of Texas), SDMA (1:1,000; Cell Signaling Technology, 13222S), asymmetrically dimethylated SMARCC1 me2a (Arg1064; 1:1,000; Cell Signaling Technology, 94962S), SMARCC1 (1:1,000; Cell Signaling Technology, 11956S), asymmetrically dimethylated PABPC1 (Arg455/Arg460; 1:1,000; Cell Signaling Technology, 3505S), and PABPC1 (1:1,000; Cell Signaling Technology, 4992S) to assess PRMT expression and function.

Antibodies against p-PRKAA/AMPK (Thr172, 1:1,000; Cell Signaling Technology, 2535S), AMPK (1:1,000; Cell Signaling Technology, 2532S), PPARGC1A/PGC-1 α (1:200; EMD Millipore, AB3242), CS/citrate synthase (1:1,000; Abcam, ab96600), and total OXPHOS (1:1,000; Abcam, ab110413) were used to examine metabolic signaling. Antibodies against PRKN/parkin (1:1,000; Cell Signaling Technology, 2132S) and BNIP3 (1:1,000; Cell Signaling Technology, 3769S) were used to investigate mitophagy. Antibodies against LC3 (1:1,000; Cell Signaling Technology, 4108S), SQSTM1/p62 (1:1,000; Sigma-Aldrich, P0067), phosphorylated ATG16L1 (Ser278, 1:1,000; Abcam, ab195242), ATG16L1 (1:1,000; Abcam, ab188642), phosphorylated MTOR (Ser2448; 1:1,000; Cell Signaling Technology, 2971S), MTOR (1:1,000; Cell Signaling Technology, 2972S), phosphorylated ULK1 (Ser555; 1:1,000; Cell Signaling Technology,

5869S), phosphorylated ULK1 (Ser757; 1:1,000; Cell Signaling Technology, 14202S), ULK1 (1:1,000; Cell Signaling Technology, 8054S), TFEB (1:1,000; Cell Signaling Technology, 4240S), SKP2 (1:1,000; Cell Signaling Technology, 4313S), BECN1 (1:1,000; Cell Signaling Technology, 3738S), LAMP1 (1:1,000; Abcam, ab24170), LAMP2 (1:1,000; Abcam, ab13524), and CTSD/cathepsin D (1:1,000; Cell Signaling Technology, 2284S) were used to evaluate autophagy.

Antibodies against TRIM63 (1:200; R&D Systems, AF5366), FBXO32/MAFbx (1:1,000; ECM Biosciences, AP2041), ubiquitin (1:500; Cell Signaling Technology, 3933S), phosphorylated AKT (Ser473; 1:1,000; Cell Signaling Technology, 9271S), AKT (1:1,000; Cell Signaling Technology, 4691S), phosphorylated FOXO1 (Ser256; 1:1,000; Cell Signaling Technology, 9461S), FOXO1 (1:1,000; Cell Signaling Technology, 2880S), phosphorylated FOXO3 (Ser253; 1:1,000; Cell Signaling Technology, 9466S), phosphorylated FOXO3 (Ser413; 1:1,000; Cell Signaling Technology, 8174S), phosphorylated FOXO3 (Ser588; 1:1,000; a kind gift from Dr. Anne Brunet, Department of Genetics, Stanford University School of Medicine), and FOXO3 (1:1,000; Cell Signaling Technology, 2497S) were employed to analyze the muscle atrophy program. We also employed antibodies against TOMM20 (1:1,000; Santa Cruz Biotechnology, sc -17,764), histone H3 (1:1,000; Abcam, ab18521), and GAPDH (glyceraldehyde-3-phosphate dehydrogenase; 1:1,000; Abcam, ab9483) to serve as markers of purity for mitochondrial, nuclear, and cytosolic fractions, respectively.

Immunoprecipitation (IP). Previously prepared whole muscle lysate and nuclear fractions from TA and GAST, respectively, were used for IP experiments. The IP procedure was carried out as described earlier [10,15,69]. For all IP experiments, 200 μg of protein was precleared with 50 μl of protein A agarose suspension (EMD Millipore, IP02) and 1 μg of rabbit Immunoglobulin G (IgG; EMD Millipore, 12-370). This was followed by end-over-end inversion for 60 min at 4°C followed by centrifugation at $12,000 \times g$ for 10 min. Precleared supernatant was then rotated by end-over-end inversion for 2 h at 4°C with anti-CARM1 (1:100; Bethyl Laboratories, A300-421A). Next, 50 μl of protein A agarose suspension was added and the samples were mixed by end-over-end inversion overnight at 4°C . The next day, agarose beads were washed five times with 500 μl of $1 \times$ PBS (137 mM NaCl, 2.7 mM KCl, 10 mM Na_2HPO_4 , 1.8 mM KH_2PO_4) and centrifuged at $12,000 \times g$. After suspending each agarose bead complex with equal volumes of $2 \times$ SDS sample buffer (50 μl ; Bio-Rad Laboratories, Inc., 1610737), samples were boiled for 5 min and centrifuged at $12,000 \times g$ for 1 min. After spinning, only the supernatants were saved for SDS-PAGE (6 μl) separation.

RNA isolation and quantitative real-time (q) RT-PCR. EDL and SOL muscles were used to isolate total RNA and perform qRT-PCR as described previously [10,15]. Samples were first homogenized in 1 mL of chilled TRIzol reagent (Thermo Fisher Scientific Life Sciences 15,596,018) using stainless steel lysing beads and TissueLyser (Qiagen, Hilden, NRW, Germany) at a frequency of 30 Hz for 5 min. This was followed by adding 200 μL of chloroform (Sigma-Aldrich, C2432), shaking vigorously for 15 s, and centrifuging at

12,000 × g for 10 min. The upper aqueous (RNA) phase was purified using the Total RNA Omega Bio-Tek kit (VWR International, Radnor, PA, USA). RNA concentration and purity were determined using the NanoDrop 1000 Spectrophotometer (Thermo Fisher Scientific Life Sciences, Waltham, MA, USA). RNA samples were then reverse-transcribed into cDNA using a high-capacity cDNA reverse transcription kit (Thermo Fisher Scientific Life Sciences 4,368,814).

All individual qRT-PCRs were run in duplicate 6 µL reactions containing GoTaq qPCR Master Mix (Promega, Madison, WI, USA). Data were analyzed using the comparative C_T method [70]. ACTB (actin beta) was used as a control housekeeping gene for all experiments. This control C_T value was subtracted from the C_T value of the gene of interest [$\Delta C_T = C_T$ (target gene) - C_T (endogenous control)]. The mean ΔC_T value from the fed WT group (WT Fed) was then subtracted from the ΔC_T values of the fed mKO muscle [$\Delta\Delta C_T = \Delta C_T$ (mKO Fed) - C_T (WT Fed)]. This calculation was then repeated for fasted WT and mKO animals. Results are reported as fold changes using the $\Delta\Delta C_T$ method, calculated as $2^{-\Delta\Delta C_T}$. The primers used in this study are shown in Table S1.

Histological analyses. H&E (hematoxylin and eosin) staining was performed on QUAD, EDL, and SOL muscle cross-sections to determine the CSA (cross-sectional area) of individual muscle fibers, as described previously [15]. Muscles were first sectioned at 5 µm using a cryostat set at -20°C (Thermo Fisher Scientific Life Sciences, Waltham, MA, USA). Muscle cross-sections were then stained with hematoxylin (Sigma-Aldrich, HHS32) and eosin (Bioshop Canada Inc., EOS109), dehydrated with successive 70%, 95%, and 100% ethanol exposures, further dried with xylene (Sigma-Aldrich 534,056) and mounted with Permount (BioWorld 21,750,009). H&E-stained muscle sections were imaged using light microscopy at 20× magnification with Nikon Elements Microscopic Imaging Software (Nikon Instruments Inc, Melville, NY, USA). The CSA of 150 myofibers across three separate regions of interest per muscle were measured (NIS-Elements). The investigators performing the image analyses were blinded to all samples.

SDH staining of EDL muscle cross-sections was carried out as described previously [15]. Briefly, muscles were cryosectioned into 8 µm slices and slides were later incubated in a buffer consisting of 0.2 M sodium succinate, 0.2 M phosphate buffer, pH 7.4, and nitro blue tetrazolium (Sigma-Aldrich, N6876) at 37°C for 1 h. Following the incubation step, muscle sections were rinsed with distilled water, exposed to 30%, 60%, and 90% acetone, and mounted with Permount (BioWorld 21,750,009). SDH-stained muscle sections were later imaged using light microscopy at 20× magnification with Nikon Elements Microscopic Imaging Software (Nikon Instruments Inc, Melville, NY, USA). SDH staining intensity was assessed by blinded investigators using ImageJ.

Preparation of permeabilized muscle fiber bundles. Permeabilization of muscle fibers was conducted as described earlier [71,72]. During tissue collection, the proximal half of the TA muscle was sectioned and immediately placed in ice-cold biopsy preservation solution (BIOPS; 10 mM Ca-EGTA solution, 5.77 mM ATP, 6.56 mM MgCl₂, 20 mM taurine, 15

mM phosphocreatine, 20 mM imidazole, 0.5 mM dithiothreitol, and 50 mM MES hydrate, pH 7.1). Once fat and connective tissue were removed, fine tip forceps were used to divide muscle fibers into small muscle bundles (~5 mg) underneath a dissection microscope while on a frozen block. The muscle bundles were then added to BIOPS solution with saponin (50 µg/µl) and mixed by end-over end inversion for 30 min at 4°C. Bundles were also treated with 2,4-dinitrochlorobenzene (CDNB; 35 µM) during permeabilization to deplete glutathione and allow for detectable rates of hydrogen peroxide (H₂O₂) emission. Following permeabilization, samples were incubated in buffer Z (105 mM K-MES, 30 mM KCl, 10 mM KH₂PO₄, 5 mM MgCl₂, 1 mM EGTA, 5 mg/mL BSA, pH 7.4) on a rotor at 4°C for at least 15 min until the respiration and H₂O₂ emission trials commenced.

Mitochondrial respiration and H₂O₂ emission. High-resolution measurements of mitochondrial oxygen consumption were assessed with the Oxygraph-2k (Oroboros Instruments, Innsbruck, Austria) as described previously [12,72]. The chambers were calibrated prior to adding 2 mL of buffer Z, blebbistatin (BLEB; 5 µM), and Amplex Red. Following permeabilization and washing, muscle bundles were blotted dry, weighed, and then placed into instrument chambers. All experiments were performed at 37°C with constant stirring at 750 rpm, and at oxygen concentrations greater than 250 nmol/mL. For ADP-stimulated respiratory kinetics, pyruvate (5 mM) and malate (2 mM) were added to stimulate complex I, followed by maximal ADP (5 mM). In the presence of complex I-specific glutamate (5 mM), succinate (20 mM) was then added to saturate electron entry into complex II. Cytochrome c (10 µM) was added last to verify mitochondrial membrane integrity, with all trials inducing < 10% increase in respiration. For analysis, oxygen flux was calculated from the derivative of the oxygen concentration in the respiratory chamber. Respiration values were then normalized to fiber bundle wet weight (pmol/sec/mg), or CS protein content determined by western blot in TA muscle sampled from the same mouse (pmol/sec/CS arbitrary units), as validated previously [71]. Mitochondrial H₂O₂ emission was measured fluorometrically using the O2k-Fluo LED2-Module (Oroboros Instruments, Innsbruck, Austria) as described previously [73]. Briefly, horseradish peroxidase (1 U/mL), superoxide dismutase (5 U/mL), and Amplex Red (10 µM) were added to convert superoxide to H₂O₂. This was accompanied by H₂O₂-mediated conversion of Amplex Red to resorufin. Fluorometric sensor calibrations were performed by adding H₂O₂ titrations (0.1–0.4 µM) before each trial. Mitochondrial H₂O₂ emission values were also normalized to fiber bundle wet weight (pmol/sec/mg), or CS protein content (pmol/sec/CS arbitrary units).

Transmission electron microscopy (TEM). Fresh TA muscle was immediately fixed in 2% (v/v) glutaraldehyde in 0.1 mol/L sodium cacodylate buffer pH 7.4 and processed as described earlier [74]. Mitochondria were then quantified as described previously [72,75]. Representative micrographs from ten unique fibers were acquired at 15,000× magnification. Each micrograph contained a portion of the subsarcolemmal region adjacent to the nucleus, with most of the image containing the intermyofibrillar area. Blinded quantification of mitochondrial size (mean area, µm²), distribution (number per µm²) and density

($\mu\text{m}^2 \times \text{number per } \mu\text{m}^2 \times 100$) was performed by manually outlining and counting mitochondria in ImageJ. Total number of abnormal mitochondria (i.e., mitochondria with disrupted membranes, loss of cristae, and vacuolization) and autophagic vacuoles were also assessed at 15,000 \times magnification [31].

Immunofluorescence (IF) microscopy. EDL muscles were cryosectioned into 8 μm sections and stained for MYH (myosin heavy chain) isoforms as described previously (6). Slides were initially blocked with 10% goat serum in PBS for 1 h, before being stained with a cocktail consisting of 10% goat serum in PBS with MYH type I (1:50; BA-F8), IIA (1:600; SC-71), IIX (1:50; 6H1) (Developmental Studies Hybridoma Bank, Iowa City, Iowa, USA), and laminin (1:500; Sigma-Aldrich, L0663) for 2 h. Muscle samples were then washed three times with 1 \times PBS for 5 min, and then incubated with a secondary antibody cocktail composed of goat-anti-mouse Alexa Fluor 350 (1:500 in PBS; Thermo Fisher Scientific Life Sciences, A-21140), goat-anti-mouse Alexa Fluor 488 (1:500 in PBS; Thermo Fisher Scientific Life Sciences, A-21121), goat-anti-mouse Alexa Fluor 555 (1:500 in PBS; Thermo Fisher Scientific Life Sciences, A-21426), and goat-anti-rat Alexa Fluor 647 (1:500 in PBS; Thermo Fisher Scientific Life Sciences, A-21247) for 1 h. Following another three washes with 1 \times PBS, slides were dried and mounted in Prolong Gold antifade reagent (Thermo Fisher Scientific Life Sciences, P36930). Images were captured at 20 \times magnification using Nikon Elements Microscopic Imaging Software (Nikon Instruments Inc, Melville, NY, USA). Blinded quantification of MYH composition was performed by manually counting MYH type I (blue), IIA (green), IIX (red), and IIB (black) muscle fibers.

The immunostaining procedure for PRKN and TOMM20 was carried out as described earlier [45]. Briefly, EDL muscles embedded in OCT were sectioned into 8 μm slices. Muscle samples were later incubated in 0.2% Triton X-100 for 30 min, 5% normal goat serum (Sigma-Aldrich, G9023) for 40 min, and then PRKN antibody (1:250; Cell Signaling Technology, 2132S) overnight at 4°C. The next day, muscle sections were incubated in TOMM20 antibody (1:50; Santa Cruz Biotechnology, sc-17,764) for 2 h at room temperature. Slides were then incubated in goat-anti-rabbit Alexa Fluor 594 (1:500; Thermo Fisher Scientific Life Sciences, A-11037) and goat-anti-mouse Alexa Fluor 488 (1:500; Thermo Fisher Scientific Life Sciences, A-11029), to visualize PRKN and TOMM20, respectively. Samples were subsequently imaged using 60 \times magnification oil immersion lens with Nikon Elements Microscopic Imaging Software (Nikon Instruments Inc, Melville, NY, USA). For analysis, 6 regions of interest (ROI) were created per animal throughout the muscle cross-section. Images of interest were quantitatively assessed for the number of PRKN puncta by a blinded researcher as previously described [45].

The IF procedure for staining p-ATG16L1 (Ser278) puncta was performed as described previously [51]. EDL muscle samples embedded in OCT were sectioned into 8 μm cross-sections. Microscope slides were then washed with 1 \times PBS for 5 min, fixed in 4% PFA for 25 min, followed by another three washes with 1 \times PBS. Samples were then treated with 3% H_2O_2 (in PBS) for 10 min, washed three times with 1 \times

TBST, blocked with 5% BSA-TBST for 2 h, before being stained with p-ATG16L1 (Ser278; 1:300 in TBST; Abcam, ab195242) and laminin (1:500 in TBST; Sigma-Aldrich, L0663) overnight at 4°C. The next day, sections were washed three times with 1 \times TBST and incubated with goat-anti-rabbit Alexa Fluor 594 (1:500 in TBST; Thermo Fisher Scientific Life Sciences, A-11037) and goat-anti-rat Alexa Fluor 647 (1:500 in TBST; Thermo Fisher Scientific Life Sciences, A-21247) for 1 h at room temperature. The slides were then washed three times with 1 \times TBST prior to being treated with 4',6-diamidino-2-phenylindole dihydrochloride (DAPI; 1:20,000 in 1% BSA in PBS; Sigma-Aldrich, D9542) for 5 min to label nuclei. After three more washes with 1 \times TBST, the slides were dried and mounted in Prolong Gold antifade reagent (Thermo Fisher Scientific Life Sciences, P36930). Images were captured with 60 \times magnification oil immersion lens using Nikon Elements Microscopic Imaging Software (Nikon Instruments Inc, Melville, NY, USA).

Myonuclear TFEB localization was examined with IF microscopy as described earlier [76,77]. EDL muscle snap frozen in OCT were cryosectioned into 8 μm slices. To avoid nonspecific binding, slides were first blocked with 5% BSA for 1 h. Slides were then incubated overnight at 4°C in a primary antibody solution targeting TFEB (1:100; Bethyl Laboratories, A303-673A). The following morning, sections were washed three times with 1 \times PBS for 10 min, exposed to goat-anti-rabbit Alexa Fluor 594 (1:500; Thermo Fisher Scientific Life Sciences, A-11037) for 2 h at room temperature, followed by another three washes with 1 \times PBS. Samples were then incubated in a fluorophore-conjugated wheat germ agglutinin (WGA) antibody (1:300; Thermo Fisher Scientific Life Sciences, W11261) for 10 min and DAPI (1:20,000; Sigma-Aldrich, D9542) in 1% BSA in 1 \times PBS for 5 min to label myonuclei. After the slides were dried, fluorescent mounting medium (Agilent Technologies, S3023) was applied to mount the slide with a cover slip. Slides were then imaged by confocal microscopy at 20 \times magnification with Nikon Elements Microscopic Imaging Software (Nikon Instruments Inc, Melville, NY, USA). For each sample, 3–4 ROI were generated to represent approximately 40% of the total muscle CSA. Myonuclear TFEB localization was then determined as the percentage of TFEB-positive myonuclei relative to total myonuclei. An average of ~900 myonuclei were counted per sample per time point. The investigators were blinded to all samples prior to commencing IF microscopy analyses.

Statistical analyses. Statistical tests were performed on the raw data prior to conversion to the -fold differences that appear in graphical summaries. A Student's t test, one-way analysis of variance (ANOVA), two-way ANOVA, and Tukey post hoc tests were employed to compare means between experimental groups, as appropriate. A one-way ANOVA was used to probe CARM1 expression in WT muscles under fed and fasted conditions. A two-way ANOVA was implemented to assess the interaction between genotype and fasting for body weight, muscle weight, myofiber CSA, mRNA and protein content, oxygen and H_2O_2 flux, as well as TEM and IF microscopy analyses. Separate two-way ANOVAs were applied to WT and mKO mice treated with saline or colchicine under fed and fasted

conditions. Unpaired *t*-tests between genotypes were carried out to compare relative -fold changes that occurred with fasting. Statistical analyses were assessed using Prism software (GraphPad Software, San Diego, CA, USA). All results are expressed as means \pm SEM and statistical differences were considered significant if $p < 0.05$.

Acknowledgements

We thank Dr. Mark Bedford (MD Anderson Cancer Center, University of Texas) and Dr. Anne Brunet (Department of Genetics, Stanford University School of Medicine) for the gifts of CARM1 floxed mice and the CARM1 substrate reagent, as well as the p-FOXO3 (Ser588) antibody, respectively. We are grateful to members of the Integrative Neuromuscular Biology Laboratory and to colleagues in the Exercise Metabolism Research Group at McMaster University for helpful advice and discussion.

Disclosure statement

No potential conflict of interest was reported by the authors.

Funding

This work was funded by the Natural Science and Engineering Research Council of Canada (NSERC), the Canada Research Chairs program, and the Ontario Ministry of Economic Development, Job Creation and Trade (MEDJCT). D.W.S., T.L.V., S.Y.N., and E.K.W. are NSERC postgraduate scholars. A.I.M. is an Ontario Graduate scholar. E.K.W. is an Interdisciplinary Fellow of the Canadian Frailty Network. V.L. is the Canada Research Chair (Tier 2) in Neuromuscular Plasticity in Health and Disease and is a MEDJCT Early Researcher.

Data availability statement

Data from this study are available from the Lead Contact, Dr. Vladimir Ljubcic (ljubicic@mcmaster.ca), upon reasonable request.

ORCID

Vladimir Ljubcic  <http://orcid.org/0000-0002-4592-4093>

References

- Bedford MT, Clarke SG. Protein arginine methylation in mammals: who, what, and why. *Mol Cell*. 2009 Jan 16;33(1):1–13. PMID: 19150423; PMCID: PMC3372459. doi: [10.1016/j.molcel.2008.12.013](https://doi.org/10.1016/j.molcel.2008.12.013).
- Yang Y, Bedford MT. Protein arginine methyltransferases and cancer. *Nat Rev Cancer*. 2013 Jan;13(1):37–50. Epub 2012 Dec 13. PMID: 23235912. doi: [10.1038/nrc3409](https://doi.org/10.1038/nrc3409)
- Fulton MD, Brown T, Zheng YG. The biological axis of protein arginine methylation and asymmetric dimethylarginine. *Int J Mol Sci*. 2019 Jul 6;20(13):3322. PMID: 31284549; PMCID: PMC6651691. doi: [10.3390/ijms20133322](https://doi.org/10.3390/ijms20133322)
- Guccione E, Richard S. The regulation, functions and clinical relevance of arginine methylation. *Nat Rev Mol Cell Biol*. 2019 Oct;20(10):642–657. Epub 2019 Jul 26. Erratum in: *Nat Rev Mol Cell Biol*. 2019 Sep;20(9):567. PMID: 31350521. doi: [10.1038/s41580-019-0155-x](https://doi.org/10.1038/s41580-019-0155-x).
- Larsen SC, Sylvestersen KB, Mund A, et al. Proteome-wide analysis of arginine monomethylation reveals widespread occurrence in human cells. *Sci Signal*. 2016 Aug 30;9(443):rs9. PMID: 27577262. doi: [10.1126/scisignal.aaf7329](https://doi.org/10.1126/scisignal.aaf7329).
- vanLieshout TL, Stouth DW, Hartel NG, et al. The CARM1 transcriptome and arginine methylproteome mediate skeletal muscle integrative biology. *Mol Metab*. 2022 Oct;64:101555. Epub 2022 Jul 21. PMID: 35872306; PMCID: PMC9379683 doi: [10.1016/j.molmet.2022.101555](https://doi.org/10.1016/j.molmet.2022.101555).
- Yadav N, Lee J, Kim J, et al. Specific protein methylation defects and gene expression perturbations in coactivator-associated arginine methyltransferase 1-deficient mice. *Proc Natl Acad Sci U S A*. 2003 May 27;100(11):6464–6468. Epub 2003 May 19. PMID: 12756295; PMCID: PMC164469. doi: [10.1073/pnas.1232272100](https://doi.org/10.1073/pnas.1232272100).
- Ljubcic V, Khogali S, Renaud JM, et al. Chronic AMPK stimulation attenuates adaptive signaling in dystrophic skeletal muscle. *Am J Physiol Cell Physiol*. 2012 Jan 1;302(1):C110–21. Epub 2011 Sep 21. PMID: 21940670. doi: [10.1152/ajpcell.00183.2011](https://doi.org/10.1152/ajpcell.00183.2011).
- Stouth DW, vanLieshout TL, Shen NY, et al. Regulation of Skeletal Muscle Plasticity by Protein Arginine Methyltransferases and Their Potential Roles in Neuromuscular Disorders. *Front Physiol*. 2017 Nov 1;8:870. PMID: 29163212; PMCID: PMC5674940. doi: [10.3389/fphys.2017.00870](https://doi.org/10.3389/fphys.2017.00870)
- Stouth DW, Manta A, Ljubcic V. Protein arginine methyltransferase expression, localization, and activity during disuse-induced skeletal muscle plasticity. *Am J Physiol Cell Physiol*. 2018 Feb 1;314(2):C177–C190. Epub 2017 Nov 1. PMID: 29092819; PMCID: PMC5866438. doi: [10.1152/ajpcell.00174.2017](https://doi.org/10.1152/ajpcell.00174.2017)
- Vanlieshout TL, Stouth DW, Tajik T, et al. Exercise-induced Protein Arginine Methyltransferase Expression in Skeletal Muscle. *Med Sci Sports Exerc*. 2018 Mar;50(3):447–457. PMID: 29112628. doi: [10.1249/MSS.0000000000001476](https://doi.org/10.1249/MSS.0000000000001476).
- Shen NY, Ng SY, Toepp SL, et al. Protein arginine methyltransferase expression and activity during myogenesis. *Biosci Rep*. 2018 Jan 10;38(1):BSR20171533. PMID: 29208765; PMCID: PMC6435512. doi: [10.1042/BSR20171533](https://doi.org/10.1042/BSR20171533).
- vanLieshout TL, Bonafiglia JT, Gurd BJ, et al. Protein arginine methyltransferase biology in humans during acute and chronic skeletal muscle plasticity. *J Appl Physiol*. 2019 Sep 1;127(3):867–880. doi: [10.1152/jappphysiol.00142.2019](https://doi.org/10.1152/jappphysiol.00142.2019) Epub 2019 Aug 1. PMID: 31369333; PMCID: PMC6766709.
- vanLieshout TL, Ljubcic V. The emergence of protein arginine methyltransferases in skeletal muscle and metabolic disease. *Am J Physiol Endocrinol Metab*. 2019 Dec 1;317(6):E1070–E1080. Epub 2019 Oct 8. PMID: 31593503. doi: [10.1152/ajpendo.00251.2019](https://doi.org/10.1152/ajpendo.00251.2019).
- Stouth DW, vanLieshout TL, Ng SY, et al. CARM1 Regulates AMPK Signaling in Skeletal Muscle. *iScience*. 2020 Nov 2;23(11):101755. PMID: 33241200; PMCID: PMC7672286. doi: [10.1016/j.isci.2020.101755](https://doi.org/10.1016/j.isci.2020.101755).
- Webb EK, Ng SY, Mikhail AI, et al. Impact of short-term, pharmacological CARM1 inhibition on skeletal muscle mass, function, and atrophy in mice. *Am J Physiol Endocrinol Metab*. 2023 Sep 1;325(3):E252–E266. Epub 2023 Jul 26. PMID: 37493245 doi: [10.1152/ajpendo.00047.2023](https://doi.org/10.1152/ajpendo.00047.2023).
- Chen SL, Loffler KA, Chen D, et al. The coactivator-associated arginine methyltransferase is necessary for muscle differentiation: CARM1 coactivates myocyte enhancer factor-2. *J Biol Chem*. 2002 Feb 8;277(6):4324–4333. Epub 2001 Nov 16. PMID: 11713257. doi: [10.1074/jbc.M109835200](https://doi.org/10.1074/jbc.M109835200).
- Kawabe Y, Wang YX, McKinnell IW, et al. Carm1 regulates Pax7 transcriptional activity through MLL1/2 recruitment during asymmetric satellite stem cell divisions. *Cell Stem Cell*. 2012 Sep 7;11(3):333–345. Epub 2012 Aug 2. PMID: 22863532; PMCID: PMC3438319 doi: [10.1016/j.stem.2012.07.001](https://doi.org/10.1016/j.stem.2012.07.001).
- Wang SC, Dowhan DH, Eriksson NA, et al. CARM1/PRMT4 is necessary for the glycogen gene expression programme in skeletal muscle cells. *Biochem J*. 2012 Jun 1;444(2):323–331. PMID: 22428544. doi: [10.1042/BJ20112033](https://doi.org/10.1042/BJ20112033).
- Chang NC, Sincennes MC, Chevalier FP, et al. The dystrophin glycoprotein complex regulates the epigenetic activation of muscle stem cell commitment. *Cell Stem Cell*. 2018 May 3;22(5):755–768. e6. Epub 2018 Apr 19. PMID: 29681515; PMCID: PMC5935555. doi: [10.1016/j.stem.2018.03.022](https://doi.org/10.1016/j.stem.2018.03.022).

- [21] Liu Y, Li J, Shang Y, et al. CARM1 contributes to skeletal muscle wasting by mediating FoxO3 activity and promoting myofiber autophagy. *Exp Cell Res*. 2019 Jan 1;374(1):198–209. Epub 2018 Nov 27. PMID: 30500392. doi: [10.1016/j.yexcr.2018.11.024](https://doi.org/10.1016/j.yexcr.2018.11.024).
- [22] Hu R, Wang MQ, Liu LY, et al. Calycosin inhibited autophagy and oxidative stress in chronic kidney disease skeletal muscle atrophy by regulating AMPK/SKP2/CARM1 signalling pathway. *J Cell Mol Med*. 2020 Oct;24(19):11084–11099. Epub 2020 Sep 10. PMID: 32910538; PMCID: PMC7576237. doi: [10.1111/jcmm.15514](https://doi.org/10.1111/jcmm.15514).
- [23] Ravel-Chapuis A, Haghandish A, Daneshvar N, et al. A novel CARM1-HuR axis involved in muscle differentiation and plasticity misregulated in spinal muscular atrophy. *Hum Mol Genet*. 2022 May 4;31(9):1453–1470. PMID: 34791230. doi: [10.1093/hmg/ddab333](https://doi.org/10.1093/hmg/ddab333).
- [24] Shin HJ, Kim H, Oh S, et al. AMPK-SKP2-CARM1 signalling cascade in transcriptional regulation of autophagy. *Nature*. 2016 Jun 23;534(7608):553–557. Epub 2016 Jun 15. PMID: 27309807; PMCID: PMC5568428. doi: [10.1038/nature18014](https://doi.org/10.1038/nature18014).
- [25] Shin HR, Kim H, Kim KI, et al. Epigenetic and transcriptional regulation of autophagy. *Autophagy*. 2016 Nov;12(11):2248–2249. Epub 2016 Aug 3. PMID: 27487449; PMCID: PMC5103355. doi: [10.1080/15548627.2016.1214780](https://doi.org/10.1080/15548627.2016.1214780).
- [26] Sandri M. Protein breakdown in muscle wasting: role of autophagy-lysosome and ubiquitin-proteasome. *Int J Biochem Cell Biol*. 2013 Oct;45(10):2121–2129. Epub 2013 May 7. PMID: 23665154; PMCID: PMC3775123. doi: [10.1016/j.biocel.2013.04.023](https://doi.org/10.1016/j.biocel.2013.04.023).
- [27] Kyriazis ID, Vassi E, Alvanou M, et al. The impact of diet upon mitochondrial physiology (review). *Int J Mol Med*. 2022 Nov;50(5):135. Epub 2022 Sep 21. PMID: 36129147; PMCID: PMC9542544. doi: [10.3892/ijmm.2022.5191](https://doi.org/10.3892/ijmm.2022.5191).
- [28] Cheng D, Vemulapalli V, Lu Y, et al. CARM1 methylates MED12 to regulate its RNA-binding ability. *Life Sci Alliance*. 2018 Sep 19;1(5):e201800117. PMID: 30456381; PMCID: PMC6238599. doi: [10.26508/lsa.201800117](https://doi.org/10.26508/lsa.201800117).
- [29] Cheng D, Gao G, Di Lorenzo A, et al. Genetic evidence for partial redundancy between the arginine methyltransferases CARM1 and PRMT6. *J Biol Chem*. 2020 Dec 11;295(50):17060–17070. Epub 2020 Oct 2. PMID: 33008887; PMCID: PMC7863876. doi: [10.1074/jbc.RA120.014704](https://doi.org/10.1074/jbc.RA120.014704).
- [30] Martínez-Redondo V, Jannig PR, Correia JC, et al. Peroxisome Proliferator-activated Receptor γ Coactivator-1 α Isoforms Selectively Regulate Multiple Splicing Events on Target Genes. *J Biol Chem*. 2016 Jul 15;291(29):15169–15184. Epub 2016 May 26. PMID: 27231350; PMCID: PMC4946932. doi: [10.1074/jbc.M115.705822](https://doi.org/10.1074/jbc.M115.705822).
- [31] Klionsky DJ, Abdel-Aziz AK, Abdelfatah S, et al. Guidelines for the use and interpretation of assays for monitoring autophagy (4th edition)1. *Autophagy*. 2021 Jan;17(1):1–382. Epub 2021 Feb 8. PMID: 33634751; PMCID: PMC7996087. doi: [10.1080/15548627.2020.1797280](https://doi.org/10.1080/15548627.2020.1797280).
- [32] Kjøbsted R, Hingst JR, Fentz J, et al. AMPK in skeletal muscle function and metabolism. *FASEB J*. 2018 Apr;32(4):1741–1777. Epub 2018 Jan 5. PMID: 29242278; PMCID: PMC5945561. doi: [10.1096/fj.201700442R](https://doi.org/10.1096/fj.201700442R).
- [33] Li C, Yu L, Xue H, et al. Nuclear AMPK regulated CARM1 stabilization impacts autophagy in aged heart. *Biochem Biophys Res Commun*. 2017 Apr 29;486(2):398–405. Epub 2017 Mar 15. PMID: 28315332. doi: [10.1016/j.bbrc.2017.03.053](https://doi.org/10.1016/j.bbrc.2017.03.053).
- [34] Yang S, Zhang J, Chen D, et al. CARM1 promotes gastric cancer progression by regulating TFE3 mediated autophagy enhancement through the cytoplasmic AMPK-mTOR and nuclear AMPK-CARM1-TFE3 signaling pathways. *Cancer Cell Int*. 2022 Mar 4;22(1):102. PMID: 35246137; PMCID: PMC8895580. doi: [10.1186/s12935-022-02522-0](https://doi.org/10.1186/s12935-022-02522-0).
- [35] Vendelbo MH, Møller AB, Christensen B, et al. Fasting increases human skeletal muscle net phenylalanine release and this is associated with decreased mTOR signaling. *PLoS One*. 2014 Jul 14;9(7):e102031. PMID: 25020061; PMCID: PMC4096723. doi: [10.1371/journal.pone.0102031](https://doi.org/10.1371/journal.pone.0102031).
- [36] Morales-Scholz MG, Wette SG, Stokie JR, et al. Muscle fiber type-specific autophagy responses following an overnight fast and mixed meal ingestion in human skeletal muscle. *Am J Physiol Endocrinol Metab*. 2022 Sep 1;323(3):E242–E253. Epub 2022 Jul 6. PMID: 35793481. doi: [10.1152/ajpendo.00015.2022](https://doi.org/10.1152/ajpendo.00015.2022).
- [37] Kunkel SD, Suneja M, Ebert SM, et al. mRNA expression signatures of human skeletal muscle atrophy identify a natural compound that increases muscle mass. *Cell Metab*. 2011 Jun 8;13(6):627–638. PMID: 21641545; PMCID: PMC3120768. doi: [10.1016/j.cmet.2011.03.020](https://doi.org/10.1016/j.cmet.2011.03.020).
- [38] Zhou K, Chen H, Lin J, et al. FGF21 augments autophagy in random-pattern skin flaps via AMPK signaling pathways and improves tissue survival. *Cell Death Dis*. 2019 Nov 18;10(12):872. PMID: 31740658; PMCID: PMC6861244. doi: [10.1038/s41419-019-2105-0](https://doi.org/10.1038/s41419-019-2105-0).
- [39] Yu YS, Shin HR, Kim D, et al. Pontin arginine methylation by CARM1 is crucial for epigenetic regulation of autophagy. *Nat Commun*. 2020 Dec 8;11(1):6297. PMID: 33293536; PMCID: PMC7722926. doi: [10.1038/s41467-020-20080-9](https://doi.org/10.1038/s41467-020-20080-9).
- [40] Triolo M, Hood DA. Manifestations of age on autophagy, Mitophagy and lysosomes in skeletal muscle. *Cells*. 2021 Apr 29;10(5):1054. PMID: 33946883; PMCID: PMC8146406. doi: [10.3390/cells10051054](https://doi.org/10.3390/cells10051054).
- [41] Milan G, Romanello V, Pescatore F, et al. Regulation of autophagy and the ubiquitin-proteasome system by the FoxO transcriptional network during muscle atrophy. *Nat Commun*. 2015 Apr 10;6:6670. PMID: 25858807; PMCID: PMC4403316. doi: [10.1038/ncomms7670](https://doi.org/10.1038/ncomms7670).
- [42] Brocca L, Toniolo L, Reggiani C, et al. FoxO-dependent atrogenes vary among catabolic conditions and play a key role in muscle atrophy induced by hindlimb suspension. *J Physiol*. 2017 Feb 15;595(4):1143–1158. Epub 2016 Dec 12. PMID: 27767211; PMCID: PMC5309360. doi: [10.1113/JP273097](https://doi.org/10.1113/JP273097).
- [43] McCarthy JJ, Srikuea R, Kirby TJ, et al. Inducible Cre transgenic mouse strain for skeletal muscle-specific gene targeting. *Skelet Muscle*. 2012;2(1):8. doi: [10.1186/2044-5040-2-8](https://doi.org/10.1186/2044-5040-2-8).
- [44] Drew AE, Moradei O, Jacques SL, et al. Identification of a CARM1 inhibitor with potent in vitro and in vivo activity in preclinical models of multiple myeloma. *Sci Rep*. 2017 Dec 21; 7(1): 17993. PMID: 29269946; PMCID: PMC5740082. doi: [10.1038/s41598-017-18446-z](https://doi.org/10.1038/s41598-017-18446-z).
- [45] Bujak AL, Crane JD, Lally JS, et al. AMPK activation of muscle autophagy prevents fasting-induced hypoglycemia and myopathy during aging. *Cell Metab*. 2015 Jun 2;21(6):883–890. PMID: 26039451; PMCID: PMC5233441. doi: [10.1016/j.cmet.2015.05.016](https://doi.org/10.1016/j.cmet.2015.05.016).
- [46] Laker RC, Drake JC, Wilson RJ, et al. Ampk phosphorylation of Ulk1 is required for targeting of mitochondria to lysosomes in exercise-induced mitophagy. *Nat Commun*. 2017 Sep 15;8(1):548. PMID: 28916822; PMCID: PMC5601463. doi: [10.1038/s41467-017-00520-9](https://doi.org/10.1038/s41467-017-00520-9).
- [47] Vainshtein A, Desjardins EM, Armani A, et al. PGC-1 α modulates denervation-induced mitophagy in skeletal muscle. *Skelet Muscle*. 2015 Mar 18;5:9. PMID: 25834726; PMCID: PMC4381453. doi: [10.1186/s13395-015-0033-y](https://doi.org/10.1186/s13395-015-0033-y).
- [48] Wang Y, Pessin JE. Mechanisms for fiber-type specificity of skeletal muscle atrophy. *Curr Opin Clin Nutr Metab Care*. 2013 May;16(3):243–250. PMID: 23493017; PMCID: PMC4327989. doi: [10.1097/MCO.0b013e328360272d](https://doi.org/10.1097/MCO.0b013e328360272d).
- [49] Hung CM, Lombardo PS, Malik N, et al. AMPK/ULK1-mediated phosphorylation of parkin ACT domain mediates an early step in mitophagy. *Sci Adv*. 2021 Apr 7;7(15):eabg4544. PMID: 33827825; PMCID: PMC8026119. doi: [10.1126/sciadv.abg4544](https://doi.org/10.1126/sciadv.abg4544).
- [50] Hood DA, Memme JM, Oliveira AN, et al. Maintenance of skeletal muscle mitochondria in Health, exercise, and aging. *Annu Rev Physiol*. 2019 Feb 10;81:19–41. Epub 2018 Sep 14. PMID: 30216742. doi: [10.1146/annurev-physiol-020518-114310](https://doi.org/10.1146/annurev-physiol-020518-114310).
- [51] Tian W, Alsaadi R, Guo Z, et al. An antibody for analysis of autophagy induction. *Nat Methods*. 2020 Feb;17(2):232–239. Epub 2019 Nov 25. PMID: 31768061. doi: [10.1038/s41592-019-0661-y](https://doi.org/10.1038/s41592-019-0661-y).
- [52] Castets P, Lin S, Rion N, et al. Sustained activation of mTORC1 in skeletal muscle inhibits constitutive and starvation-induced autophagy and causes a severe, late-onset myopathy. *Cell Metab*. 2013

- May 7;17(5):731–744. Epub 2013 Apr 18. PMID: 23602450. [10.1016/j.cmet.2013.03.015](https://doi.org/10.1016/j.cmet.2013.03.015).
- [53] Napolitano G, Esposito A, Choi H, et al. mTOR-dependent phosphorylation controls TFEB nuclear export. *Nat Commun*. 2018 Aug 17;9(1):3312. PMID: 30120233; PMCID: PMC6098152 doi: [10.1038/s41467-018-05862-6](https://doi.org/10.1038/s41467-018-05862-6).
- [54] Markby GR, Sakamoto K. Transcription factor EB and TFE3: new metabolic coordinators mediating adaptive responses to exercise in skeletal muscle? *Am J Physiol Endocrinol Metab*. 2020 Oct 1;319(4):E763–E768. Epub 2020 Aug 24. PMID: 32830550. [10.1152/ajpendo.00339.2020](https://doi.org/10.1152/ajpendo.00339.2020)
- [55] Martina JA, Diab HI, Lishu L, et al. The nutrient-responsive transcription factor TFE3 promotes autophagy, lysosomal biogenesis, and clearance of cellular debris. *Sci Signal*. 2014 Jan 21;7(309):ra9. PMID: 24448649; PMCID: PMC4696865. [10.1126/scisignal.2004754](https://doi.org/10.1126/scisignal.2004754).
- [56] Pastore N, Vainshtein A, Klish TJ, et al. TFE3 regulates whole-body energy metabolism in cooperation with TFEB. *EMBO Mol Med*. 2017 May;9(5):605–621. PMID: 28283651; PMCID: PMC5412821. doi: [10.15252/emmm.201607204](https://doi.org/10.15252/emmm.201607204).
- [57] Paquette M, El-Houjeiri L, Zirden C, et al. AMPK-dependent phosphorylation is required for transcriptional activation of TFEB and TFE3. *Autophagy*. 2021 Mar;18:1–19. doi: [10.1080/15548627.2021.1898748](https://doi.org/10.1080/15548627.2021.1898748). Epub ahead of print. PMID: 33734022
- [58] Sartori R, Romanello V, Sandri M. Mechanisms of muscle atrophy and hypertrophy: implications in health and disease. *Nat Commun*. 2021 Jan 12;12(1):330. PMID: 33436614; PMCID: PMC7803748. doi: [10.1038/s41467-020-20123-1](https://doi.org/10.1038/s41467-020-20123-1).
- [59] Calnan DR, Brunet A. The FoxO code. *Oncogene*. 2008 Apr 7;27(16):2276–2288. PMID: 18391970. doi: [10.1038/onc.2008.21](https://doi.org/10.1038/onc.2008.21).
- [60] Sanchez AM, Candau RB, Bernardi H. FoxO transcription factors: their roles in the maintenance of skeletal muscle homeostasis. *Cell Mol Life Sci*. 2014 May;71(9):1657–1671. PMID: 24232446. doi: [10.1007/s00018-013-1513-z](https://doi.org/10.1007/s00018-013-1513-z).
- [61] Greer EL, Oskoui PR, Banko MR, et al. The energy sensor AMP-activated protein kinase directly regulates the mammalian FOXO3 transcription factor. *J Biol Chem*. 2007 Oct 12;282(41):30107–30119. Epub 2007 Aug 20. PMID: 17711846. [10.1074/jbc.M705325200](https://doi.org/10.1074/jbc.M705325200).
- [62] Bao J, Rousseaux S, Shen J, et al. The arginine methyltransferase CARM1 represses p300•ACT•CREM τ activity and is required for spermiogenesis. *Nucleic Acids Res*. 2018 May 18;46(9):4327–4343. PMID: 29659998; PMCID: PMC5961101. [10.1093/nar/gky240](https://doi.org/10.1093/nar/gky240).
- [63] Edgett BA, Hughes MC, Matusiak JB, et al. SIRT3 gene expression but not SIRT3 subcellular localization is altered in response to fasting and exercise in human skeletal muscle. *Exp Physiol*. 2016 Aug 1;101(8):1101–1113. Erratum in: *Exp Physiol*. 2016 Oct 1;101(10):1319. PMID: 27337034. doi: [10.1113/EP085744](https://doi.org/10.1113/EP085744)
- [64] Edgett BA, Scribbans TD, Raleigh JP, et al. The impact of a 48-h fast on SIRT1 and GCN5 in human skeletal muscle. *Appl Physiol Nutr Metab*. 2016 Sep;41(9):953–962. Epub 2016 May 5. PMID: 27525514. doi: [10.1139/apnm-2016-0130](https://doi.org/10.1139/apnm-2016-0130).
- [65] Ju JS, Varadhachary AS, Miller SE, et al. Quantitation of “autophagic flux” in mature skeletal muscle. *Autophagy*. 2010 Oct;6(7):929–935. Epub 2010 Oct 24. PMID: 20657169; PMCID: PMC3039739. doi: [10.4161/auto.6.7.12785](https://doi.org/10.4161/auto.6.7.12785).
- [66] Carter HN, Kim Y, Erlich AT, et al. Autophagy and mitophagy flux in young and aged skeletal muscle following chronic contractile activity. *J Physiol*. 2018 Aug;596(16):3567–3584. Epub 2018 Jul 3. PMID: 29781176; PMCID: PMC6092298. doi: [10.1113/JP275998](https://doi.org/10.1113/JP275998).
- [67] Dimauro I, Pearson T, Caporossi D, et al. A simple protocol for the subcellular fractionation of skeletal muscle cells and tissue. *BMC Res Notes*. 2012 Sep 20;5:513. PMID: 22994964; PMCID: PMC3508861. doi: [10.1186/1756-0500-5-513](https://doi.org/10.1186/1756-0500-5-513)
- [68] Romero-Calvo I, Ocón B, Martínez-Moya P, et al. Reversible Ponceau staining as a loading control alternative to actin in Western blots. *Anal Biochem*. 2010 Jun 15;401(2):318–320. Epub 2010 Mar 3. PMID: 20206115. [10.1016/j.ab.2010.02.036](https://doi.org/10.1016/j.ab.2010.02.036).
- [69] Philp A, Chen A, Lan D, et al. Sirtuin 1 (SIRT1) deacetylase activity is not required for mitochondrial biogenesis or peroxisome proliferator-activated receptor-gamma coactivator-1alpha (PGC-1alpha) deacetylation following endurance exercise. *J Biol Chem*. 2011 Sep 2;286(35):30561–30570. Epub 2011 Jul 11. PMID: 21757760; PMCID: PMC3162416. [10.1074/jbc.M111.261685](https://doi.org/10.1074/jbc.M111.261685).
- [70] Schmittgen TD, Livak KJ. Analyzing real-time PCR data by the comparative C(T) method. *Nat Protoc*. 2008;3(6):1101–1108. PMID: 18546601. doi: [10.1038/nprot.2008.73](https://doi.org/10.1038/nprot.2008.73)
- [71] Kuznetsov AV, Veksler V, Gellerich FN, et al. Analysis of mitochondrial function in situ in permeabilized muscle fibers, tissues and cells. *Nat Protoc*. 2008;3(6):965–976. PMID: 18536644 doi: [10.1038/nprot.2008.61](https://doi.org/10.1038/nprot.2008.61).
- [72] Hughes MC, Ramos SV, Turnbull PC, et al. Early myopathy in Duchenne muscular dystrophy is associated with elevated mitochondrial H₂O₂ emission during impaired oxidative phosphorylation. *J Cachexia Sarcopenia Muscle*. 2019 Jun;10(3):643–661. Epub 2019 Apr 2. PMID: 30938481; PMCID: PMC6596403. doi: [10.1002/jcsm.12405](https://doi.org/10.1002/jcsm.12405).
- [73] Buch BT, Halling JF, Ringholm S, et al. Colchicine treatment impairs skeletal muscle mitochondrial function and insulin sensitivity in an age-specific manner. *FASEB J*. 2020 Jun;34(6):8653–8670. Epub 2020 May 5. PMID: 32372536. doi: [10.1096/fj.201903113RR](https://doi.org/10.1096/fj.201903113RR).
- [74] Nilsson MI, MacNeil LG, Kitaoka Y, et al. Combined aerobic exercise and enzyme replacement therapy rejuvenates the mitochondrial-lysosomal axis and alleviates autophagic blockage in pompe disease. *Free Radic Biol Med*. 2015 Oct;87:98–112. Epub 2015 May 19. PMID: 26001726. doi: [10.1016/j.freeradbiomed.2015.05.019](https://doi.org/10.1016/j.freeradbiomed.2015.05.019)
- [75] Monaco CMF, Hughes MC, Ramos SV, et al. Altered mitochondrial bioenergetics and ultrastructure in the skeletal muscle of young adults with type 1 diabetes. *Diabetologia*. 2018 Jun;61(6):1411–1423. Epub 2018 Apr 18. Erratum in: *Diabetologia*. 2020 Apr;63(4):887–888. PMID: 29666899. doi: [10.1007/s00125-018-4602-6](https://doi.org/10.1007/s00125-018-4602-6).
- [76] Spaulding HR, Kelly EM, Quindry JC, et al. Autophagic dysfunction and autophagosome escape in the mdx mus musculus model of Duchenne muscular dystrophy. *Acta Physiol (Oxf)*. 2018 Feb;222(2). Epub 2017 Sep 20. PMID: 28834378. [10.1111/apha.12944](https://doi.org/10.1111/apha.12944)
- [77] Ng SY, Mikhail A, Ljubicic V. Mechanisms of exercise-induced survival motor neuron expression in the skeletal muscle of spinal muscular atrophy-like mice. *J Physiol*. 2019 Sep;597(18):4757–4778. Epub 2019 Aug 22. PMID: 31361024; PMCID: PMC6767691. doi: [10.1113/JP278454](https://doi.org/10.1113/JP278454).